Towards two-dimensional optics

Ziyu Gu
Student No. 0714828
Supervisor: Dr. Martin P. van Exter
September 25, 2009

Quantum Optics and Quantum Information
Leiden Institute of Physics (LION)
Leiden University

Contents

1 Introduction **4**

2 Theory of slab waveguide **5**
2.1 Electromagnetic Approach to 2-Dimensional Waveguide . . . 5
2.1.1 Maxwell's Equations Inside Matter . . . 5
2.1.2 Wave Propagation in Slab Waveguide . . . 6
2.1.3 TE Wave . . . 6
2.2 Ray Approach to 2D Waveguide . . . 8
2.2.1 Decomposition of The Wave Vector . . . 8
2.2.2 Phase Shift of Reflection . . . 9
2.2.3 Modes of a Waveguide . . . 9
2.3 Single Mode Waveguide . . . 10
2.3.1 Symmetrical Planar Waveguide . . . 10
2.3.2 Asymmetrical Planar Waveguide . . . 10
2.4 Thickness Calculation of The Core Layer . . . 11
2.4.1 Propagation Constant & Effective Refractive Index . . . 12

3 Characterization of Waveguides **13**
3.1 Designed Planar Waveguide Structure . . . 13
3.2 Microscope Observation . . . 13
3.2.1 Calibration of optical microscope . . . 13
3.2.2 Measurement of height profile . . . 16
3.2.3 Facet observation . . . 23
3.3 Conclusions of 2-D Waveguide . . . 24
3.4 Characterization of 1-D Rib Waveguide . . . 26
3.4.1 Designed Waveguide Structure . . . 26
3.4.2 Quality and Size Inspection . . . 26
3.4.3 A noticeable structure at the end face . . . 28
3.5 The Test Waveguide . . . 30
3.5.1 Measurement of stepwise height variation . . . 30

4 Experiments on in- and out-coupling for waveguides **33**
4.1 Coupling Methods . . . 33
4.2 In-coupling system . . . 34
4.2.1 Measurement of focus size . . . 34
4.2.2 Location of the Focus of the In-coupling Beam . . . 38
4.3 Out-coupling system . . . 39
4.4 Experiment result . . . 39
4.4.1 Lloyd's mirror . . . 39
4.4.2 Tilted waveguide and razer blade . . . 40
4.5 conclusion . . . 40
4.6 Suggestions . . . 41

5 Experiment on 1-dimensional waveguides **42**
5.1 Complemental theory on rib waveguide 42
5.1.1 Effective index method 42
5.1.2 Theory of single-mode rib waveguide with micron scale. 42
5.2 Optical system for rib waveguide 43
5.3 Detection of the Rib Structure 44
5.4 Modified in-coupling system 47
5.5 Modified Illumination System 47
5.6 Result obtained by the out-coupling system 49
5.7 Large Single-mode Rib Waveguide 50
5.7.1 Success in the large scale waveguide 50

6 Summary **54**

Chapter 1

Introduction

Optical waveguides are important compnents of integrated optics. The optical fiber, which is essential for telecommunication, is an example of a 1-D waveguide structure. Two-dimensional waveguides perforated with regular arrays of holes are a popular research topic in the field of photonic crystals. High-finesse cavities can be build around designed defects in such crystals. Still, the optical properties of the fundamental building block – scatter of single hole in film – are hardly known. Although not relevant in ideal photonic crystals, this scattering is very relevant in modified crystals. The goal of this master project is to acquire theoretical and experimental knowledge about waveguide technology. More specifically, we want to confine light in a two-dimensional waveguide structure, which will allow experiments with 2-D optics. A study of scattering on a single hole or several holes inside the free-standing film would be a future project. If the refractive index n of the free-standing film is large, most of the scattering will remain inside the slab waveguide, making it a good geometry to study 2-D scattering.

Chapter 2

Theory of slab waveguide

2.1 Electromagnetic Approach to 2-Dimensional Waveguide

2.1.1 Maxwell's Equations Inside Matter

The differential form of the Maxwell's equations are:

$$\begin{aligned}
\nabla \times \overrightarrow{E}(\overrightarrow{r},t) &= -\frac{\partial \overrightarrow{B}(\overrightarrow{r},t)}{\partial t} && \text{(Faraday's law)} \\
\nabla \times \overrightarrow{H}(\overrightarrow{r},t) &= \frac{\partial \overrightarrow{D}(\overrightarrow{r},t)}{\partial t} + \overrightarrow{J}(\overrightarrow{r},t) && \text{(Ampère's law)} \\
\nabla \cdot \overrightarrow{D}(\overrightarrow{r},t) &= \rho_e(\overrightarrow{r},t) && \text{(Gauss' Law)} \\
\nabla \cdot \overrightarrow{B}(\overrightarrow{r},t) &= 0 && \text{(Gauss' Law of Magnetic field)}
\end{aligned} \tag{2.1}$$

where $\overrightarrow{E}$ is electric field; $\overrightarrow{H}$ is magnetic field; $\overrightarrow{D}$ is electric flux density; $\overrightarrow{B}$ magnetic flux density; $\overrightarrow{J}$ electric current density and ρ_e is electric charge density.

Relation between the flux density and field are:

$$\overrightarrow{D} = \epsilon \overrightarrow{E}, \qquad \overrightarrow{B} = \mu \overrightarrow{H}$$

where $\epsilon = \epsilon_0 \epsilon_r$ is the permittivity and $\mu = \mu_0 \mu_r$ is the permeability of the material.

Additionally, in homogeneous dielectric material, where there is neither electric source nor current inside, $\overrightarrow{J}$ and ρ_e should both be 0, and ϵ and μ is constant. So equation (2.1) becomes:

$$\begin{aligned}
\nabla \times \overrightarrow{E}(\overrightarrow{r},t) &= -\mu \frac{\partial \overrightarrow{H}(\overrightarrow{r},t)}{\partial t} \\
\nabla \times \overrightarrow{H}(\overrightarrow{r},t) &= \epsilon \frac{\partial \overrightarrow{E}(\overrightarrow{r},t)}{\partial t} \\
\nabla \cdot (\overrightarrow{E})(\overrightarrow{r},t) &= 0 \\
\nabla \cdot (\overrightarrow{H})(\overrightarrow{r},t) &= 0
\end{aligned} \tag{2.2}$$

Taking curl of the first equation of (2.2), and substituting the second one,

$$\nabla \times \nabla \times \overrightarrow{E} = -\mu \frac{\partial}{\partial t}(\nabla \times \overrightarrow{H}) = -\mu\epsilon \frac{\partial^2 \overrightarrow{E}}{\partial t^2} \tag{2.3}$$

Using the identity $\nabla \times \nabla \times \overrightarrow{E} = \nabla(\nabla \cdot \overrightarrow{E}) - \nabla^2 \overrightarrow{E}$, equation above becomes

$$\nabla^2\overrightarrow{E} - \mu\epsilon\frac{\partial^2\overrightarrow{E}}{\partial t^2} = \nabla(\nabla\cdot\overrightarrow{E}) = 0 \tag{2.4}$$

Writing the electric field as

$$\overrightarrow{E}(\overrightarrow{r},t) = \overrightarrow{E}(\overrightarrow{r})e^{-i\omega t} \tag{2.5}$$

the equation (2.4) becomes

$$\nabla^2\overrightarrow{E}(\overrightarrow{r}) + k_0^2 n^2\overrightarrow{E}(\overrightarrow{r}) = 0 \tag{2.6}$$

where $k_0 = 2\pi/\lambda$ is the wave number in free space, and $n = \sqrt{\epsilon_r\mu_r}$ is the refractive index of the material.

2.1.2 Wave Propagation in Slab Waveguide

The model of the slab waveguide is sketched in Fig. 2.1. The waveguide consists of three planar layers, which are parallel to the xy plane. The layer with higher refractive index is sandwiched by two layers with lower refractive index ($n_2 > n_1$, $n_2 > n_3$, and generally $n_3 \geq n_1$). The waveguide is assumed to extend to infinity in y direction. We assume the light wave propagates in the z direction and write $E(\overrightarrow{r}) = E(x,y)e^{i\beta z}$, β being the propagation constant in z direction. Rewriting equation (2.6) as a function of cartesian coordinates, we find

$$(\frac{\partial^2}{\partial x^2} + \frac{\partial^2}{\partial y^2})\overrightarrow{E}(x,y) + (k_0^2 n^2 - \beta^2)\overrightarrow{E}(x,y) = 0 \tag{2.7}$$

Since the planar waveguide is assumed to be infinite in the y direction, the field is uniform in this direction ($\partial/\partial y = 0$)[1]. Substitute this operator into equation (2.7),

$$\frac{\partial^2}{\partial x^2}\overrightarrow{E}(x,y) + (k^2 n^2 - \beta^2)\overrightarrow{E}(x,y) = 0 \tag{2.8}$$

Writing this equation in 3 layers separately yield

$$\frac{\partial^2}{\partial x^2}\overrightarrow{E}(x,y) + (k_0^2 n_i^2 - \beta^2)\overrightarrow{E}(x,y) = 0 \tag{2.9}$$

where, $i = 1, 2, 3$ for layer 1, 2, and 3 from top to bottom.

2.1.3 TE Wave

The TE wave is a electromagnetic field such that the electric field has only y direction component. So the electric field is always perpendicular to the plane of the paper and parallel to the interface of the layers of the slab waveguide. (See Fig. 2.1)

In this case, $\overrightarrow{E} = E_y\hat{j}$, hence the equation (2.9) can be reduced to

$$\frac{\partial^2 E_y(x)}{\partial x^2} = (\beta^2 - k_0^2 n_i^2)E_y(x) \tag{2.10}$$

The necessary condition for the electromagnetic waveguide to guide a wave with a certain wave vector β is that kn_1, $kn_3 < \beta < kn_2$.[1] Accordingly, in the upper cladding layer, where $\beta^2 - k^2 n_1^2 > 0$, the general solution to the second order differential equation (2.10) is

$$E_y(x) = a_1 \cdot e^{\sqrt{\beta^2 - k_0^2 n_1^2}\cdot x} + a_2 \cdot e^{-\sqrt{\beta^2 - k_0^2 n_1^2}\cdot x} \tag{2.11}$$

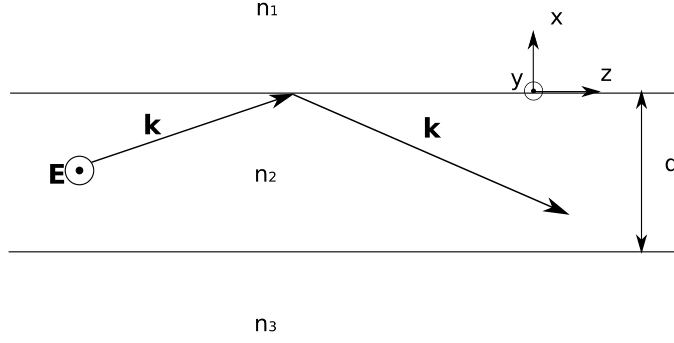

Figure 2.1: A slab waveguide with three layers, the refractive indexes of which are n_1, n_2, n_3 from top to bottom.($n_2 > n_1$, $n_2 > n_3$, and normally $n_3 \geq n_1$). TE wave propagates in a slab waveguide. The bold letters E and k indicate that the electric field and the wave vector are vectors. The thickness of layer 2 is indicated as d

And in the core layer, since $\beta^2 - k_0^2 n_2^2 < 0$,

$$E_y(x) = b_1 \cdot cos(\sqrt{k_0^2 n_2^2 - \beta^2} \cdot x) + b_2 \cdot sin(\sqrt{k_0^2 n_2^2 - \beta^2} \cdot x) \tag{2.12}$$

The condition in the lower cladding layer is the same as that in the upper cladding one (only the index is different), thus

$$E_y(x) = c_1 \cdot e^{\sqrt{\beta^2 - k_0^2 n_3^2} \cdot x} + c_2 \cdot e^{-\sqrt{\beta^2 - k_0^2 n_3^2} \cdot x} \tag{2.13}$$

By setting the origin of the coordinates on the intersection of the layer 1 and 2, and by applying the condition such that the electric field should be 0 when x goes to both $+\infty$ and $-\infty$, we find[1]

$$E_y(x) = \begin{cases} a_2 e^{-qx} & 0 \leq x < \infty \\ b_1 cos(hx) + b_2 sin(hx) & -d \leq x \leq 0 \\ c_1 e^{px} & -\infty < x \leq -d \end{cases} \tag{2.14}$$

where

$$q = \sqrt{\beta^2 - k_0^2 n_1^2}$$
$$h = \sqrt{k_0^2 n_2^2 - \beta^2}$$
$$p = \sqrt{\beta^2 - k_0^2 n_3^2}$$

Applying the boundary condition[4] that E_y is continuous at both $x = 0$ and $x = -d$, and $H_z = (i/\omega\mu)(\partial E_y/\partial x)$ is continuous at $x = 0$, equation (2.14) becomes

$$E_y(x) = \begin{cases} C\,exp(-qx) & 0 \leq x < \infty \\ C\,[cos(hx) - (q/h)\,sin(hx)] & -d \leq x \leq 0 \\ C\,[cos(hd) + (q/h)\,sin(hd)]\,exp[p(x+d)] & -\infty < x \leq -d \end{cases} \tag{2.15}$$

By applying the final continuity condition on $\partial E_y/\partial x$ at $x = -d$, we can get a transcendental equation[1]

$$h\,sin(hd) - q\,cos(hd) = p\,[cos(hd) + \frac{q}{h}\,sin(ht)]$$

or

$$tan(hd) = \frac{q+p}{h(1 - \frac{pq}{h^2})} \tag{2.16}$$

This equation can be solved numerically for a three-layer structure with known refractive indices and a given optical wavelength. By plotting both the right-hand side and left-hand side of the transcendental equation with respect to β, the horizontal value of the intersections of these curves are the possible value of propagation constant β. The result can be conveniently expressed as the effective refractive

index $n_{eff} = \frac{\beta}{\omega_0 c}$ of the waveguide mode, which is the ratio of light velocity in free space to velocity in the waveguide.

$$n_{eff} = \frac{c}{v} = \frac{\beta}{k_0} \tag{2.17}$$

2.2 Ray Approach to 2D Waveguide

2.2.1 Decomposition of The Wave Vector

Unlike the electromagnetic approach, the ray approach, which treats the light as a plane waveguide propagating inside the layer 2 at angle θ with respect to the z axis, is more intuitive. As mentioned in the previous section, the refractive indexes of the upper and lower cladding layers (n_1, n_3) are lower than that of the core (n_2). If θ is small enough, total internal reflection will occur and the light will be guided inside the core. (See Fig. 2.2)

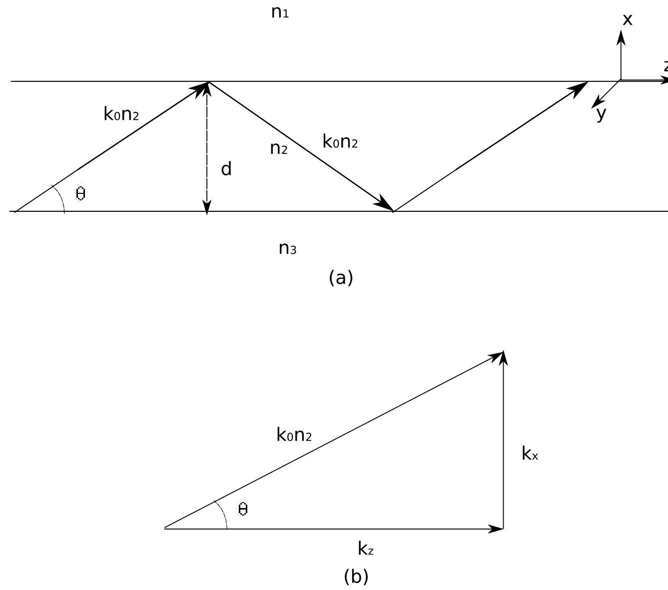

Figure 2.2: (a) A ray approach to a slab waveguide. The ray travels inside the waveguide at an angle θ with respect to the z direction. (b) Decomposition of the wave vector k.

Decompose the wave vector $\overrightarrow{k_0 n_2}$ to the x and z direction, then the x component is $k_x = n_2 k_0 sin\theta$, and z component $k_z = n_2 k_0 cos\theta$. The wave can be treated as if it propagates only in the z direction, so k_z, which indicates the rate the wave propagates in the z direction, is the propagation constant β in Section 2.1.2. And the effective refractive index n_{eff} can be calculated by $n_{eff} = n_2 cos\theta$. In terms of the x direction, the wave is reflected by the upper and lower interfaces and forms a *standing wave*. So the phase shift in the x direction for one complete "round trip" can be written as

$$\Phi = 2k_x d - \phi_u - \phi_l = 2k_0 n_2 d sin\theta - \phi_u - \phi_l \tag{2.18}$$

where ϕ_u and ϕ_l indicates the the phase shift because of the reflection on the upper and lower interface respectively.

2.2.2 Phase Shift of Reflection

In Fig 2.3, the reflection coefficient for TE polarization r_{TE} can be written as

$$r_{TE} = \frac{n_1 cos\theta_1 - n_2 cos\theta_2}{n_1 cos\theta_1 + n_2 cos\theta_2} \tag{2.19}$$

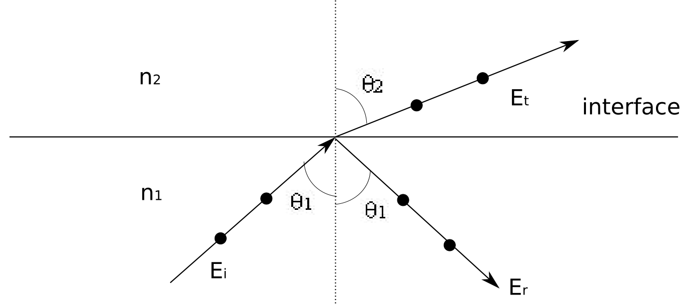

Figure 2.3: Reflection and refraction of the transverse electronic (indicated in black dots) beam from denser material to sparser one($n_1 > n_2$).

According to Snell's law: $n_1 sin\theta_1 = n_2 sin\theta_2$, and r_{TE} becomes

$$r_{TE} = \frac{n_1 cos\theta_1 - \sqrt{n_2^2 - n_1^2 sin^2\theta_1}}{n_1 cos\theta_1 + \sqrt{n_2^2 - n_1^2 sin^2\theta_1}} \tag{2.20}$$

Under the total internal reflection condition, where θ_1 is larger than the critical angle θ_c, the square root part of equation (2.20) becomes imaginary, so the reflection coefficient is a complex parameter, and the absolute value of it is equal to 1, because

$$|n_1 cos\theta_1 - \sqrt{n_2^2 - n_1^2 sin^2\theta_1}| = |n_1 cos\theta_1 + \sqrt{n_2^2 - n_1^2 sin^2\theta_1}|$$

Hence the reflection coefficient can be denoted by $r = exp(i\phi)$, where ϕ is the phase shift of the electronic field because of total internal reflection. And the phase shift can be written by:

$$\phi_{TE} = 2arctan\frac{\sqrt{sin^2\theta_1 - (\frac{n_2}{n_1})^2}}{cos\theta_1} \tag{2.21}$$

2.2.3 Modes of a Waveguide

According to the self-consistency condition [3], the total phase shift of one complete round trip of the light should be an integral times of 2π, otherwise a "standing wave" can not be formed.

$$2k_0 n_2 d sin\theta - \phi_u - \phi_l = 2m\pi \tag{2.22}$$

where $m = 0, 1, 2, 3 \ldots$.

Knowing the refractive indexes of three layers and the wavelength of the electromagnetic wave, and substituting equation (2.21) into (2.22), the latter equation, which has only one unknown parameter θ, can be solved. Because m could be any possible integer (non-negative), there are a series of discrete value of the angle θ corresponding to different value of m. Since the propagation constant depends on θ ($\beta = k_z = k_0 n_2 cos\theta$), its value is discrete as well. That means the light can not propagate inside the waveguide at any angle, but only at one (or a few) of the allowed angles. The possible solution to equation (2.22) is defined as the mode of propagation and the integral value of m is referred to the

mode number. For example, when $m = 0$, it is called the first mode or fundamental mode and when $m = 1$, it is called the second order mode.

Note that there should be no difference between the equation (2.16) and (2.22), and hence the electromagnetic approach and ray approach. Rewriting the latter equation in the tangent form, we obtain

$$tan(2k_0n_2dsin\theta - 2m\pi) = tan(\phi_u + \phi_l) = \frac{tan\phi_u + tan\phi_l}{1 - tan\phi_u \cdot tan\phi_l} \quad (2.23)$$

which has exactly the same form as equation (2.16).

2.3 Single Mode Waveguide

A single-mode waveguide is a waveguide where only the fundamental mode ($m = 0$) can propagate inside. This implies that solutions to equation (2.22) only exists when $m = 0$.

Substituting equation (2.21) into (2.22) (notice that θ in (2.22) is equal to $\pi/2 - \theta_1$ in (2.21)), so the equation becomes

$$k_0n_2dcos\theta_1 - m\pi = \phi_u + \phi_l = tan^{-1}[\frac{\sqrt{sin^2\theta_1 - (n_3/n_2)^2}}{cos\theta_1}] + tan^{-1}[\frac{\sqrt{sin^2\theta_1 - (n_1/n_2)^2}}{cos\theta_1}] \quad (2.24)$$

2.3.1 Symmetrical Planar Waveguide

A symmetrical planar waveguide is a particular type of waveguide such that the core is sandwiched by the same material, making $n_1 = n_3$. Hence equation (2.24) could be simplified as

$$tan(\frac{1}{2}k_0n_2dcos\theta_1 - m\frac{\pi}{2}) = \sqrt{\frac{cos^2\theta_c}{cos^2\theta_1} - 1}, \quad (2.25)$$

Where $sin\theta_c = n_1/n_2$.

This equation can be solved graphically. The left hand side of equation (2.25) is a periodic function (for different value of m) with respect to $cos\theta_1$, the period of which is $\frac{\pi}{k_0n_2d} = \frac{\lambda_0}{2n_2d}$. The right hand side, however, shows a decay with respect to $cos\theta_1$, ended at the critical angle θ_c (See Fig. 2.4)[3]. According to this figure, the number of intersects between the curves of LHS and RHS can be determined by modifying the value of period ($\frac{\lambda_0}{2n_2d}$) and modifying the critical angle θ_c. keeping the refractive indexes unchanged, for example, the thinner the core and/or the larger the wavelength, the fewer modes can exist. If we choose the thickness of the core extremely small (typically, in the order of hundreds of nanometer), there will be only the fundamental mode, which is allowed inside the waveguide, and the other higher-order modes are cutoff. Accordingly, the single mode waveguide can be designed. However, because dashed curve starts from $(0,+\infty)$ to $(\cos\theta_c, 0)$, and the first solid curve ($m = 0$) goes from $(0, 0)$ to $(\frac{\lambda_0}{2n_2d}, +\infty)$, no matter how thin the core is, there should be at least one mode. This is the particular case for symmetrical waveguide. For asymmetrical waveguide, which will be described below, the fundamental mode can also be cutoff.

2.3.2 Asymmetrical Planar Waveguide

In terms of asymmetrical planar waveguide ($n_1 \neq n_3$), the fundamental mode will be cutoff if the the core is too thin (d is too small), and/or if the refractive index difference between the core and the

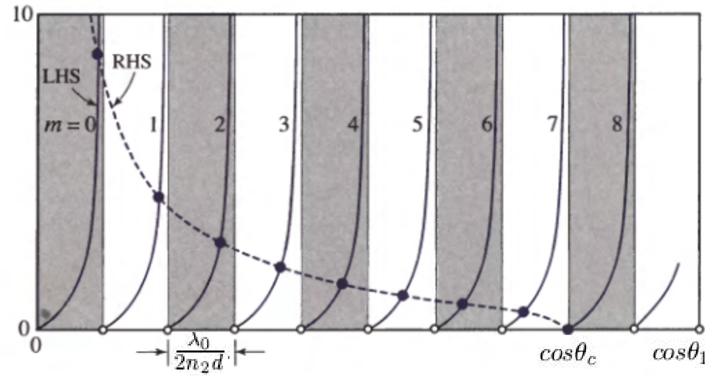

Figure 2.4: The periodic solid curves represents the LHS of equation (2.25) *whilst the dashed decay curve represents the RHD of it. The intersects of these two curves are roots of equation* (2.25)*. The number of the roots (intersects) indicates the number of the modes which can be guided inside the waveguide.[3]*

cladding material is too small. Take $n_1 = 1.4$, $n_2 = 1.5$, $n_3 = 1.49$, $\lambda_0 = 1.3\,um$, and $d = 0.3\,um$ for example. The graphical solution to the equation (2.24) for $m = 0$ in this case is shown in Fig 2.5.[5] From this figure, we can see that the solution of the angle θ_1 for $m = 0$ is smaller than the critical angle θ_l, which means total internal reflection can not occur at the lower interface, so even the fundamental mode can not exist inside this kind of waveguide.

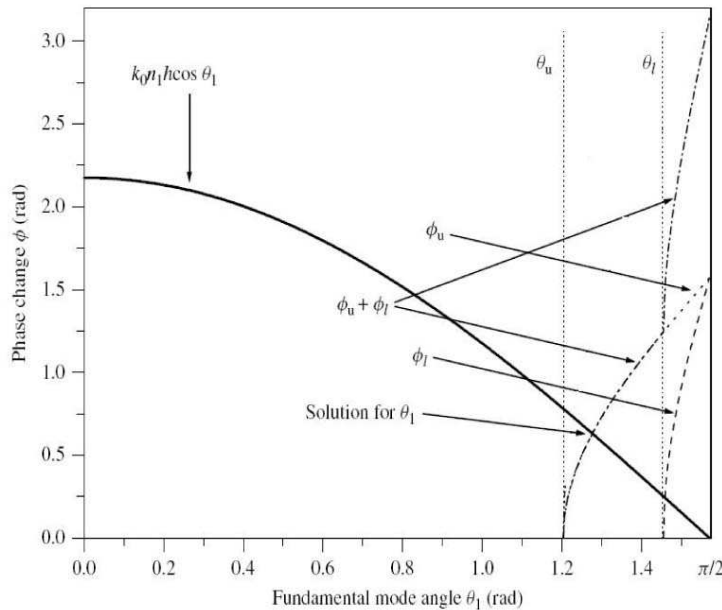

Figure 2.5: Solution of the equation (2.24) *for $m = 0$. θ_u is the critical angle between the core and the upper cladding layer, whilst θ_l being that between the core and lower cladding layer.[5]*

2.4 Thickness Calculation of The Core Layer

In this project, we chose Silicon Nitride as the core, and Silicon Dioxide as the lower cladding layer. The upper cladding layer is the air itself. The wavelength of the laser source we used is approximately 830 nm. The reflective index (at this wavelength) from top to bottom is 1, 2.187 and 1.453 (the last two numbers are given by Dr. Gregory Pandraud from Delft University of Technology who made the waveguide). To make it a single mode waveguide, the thickness of the middle layer have to be

calculated. In principle, the core should be thin enough such that second order mode ($m = 1$) is cutoff. The limiting condition for this mode is that $\theta_1 = \theta_l$, thus $sin\theta_1 = sin\theta_l = n_3/n_2 \approx 0.664$. Substituting the known data into equation (2.24),

$$d = \frac{tan^{-1}[\frac{\sqrt{sin^2\theta_l - (n_3/n_2)^2}}{cos\theta_l}] + tan^{-1}[\frac{\sqrt{sin^2\theta_l - (n_1/n_2)^2}}{cos\theta_l}] + \pi}{k_0 n_2 cos\theta_l} \quad (2.26)$$

$$= \frac{tan^{-1}[\frac{\sqrt{sin^2\theta_l - (n_1/n_2)^2}}{cos\theta_l}] + \pi}{k_0 n_2 cos\theta_l} \quad (2.27)$$

$$\approx 333\,nm \quad (2.28)$$

Recalling that the thinner the core the fewer modes can be allowed, we could claim that waveguide, which has the structure of SiN on top of SiO_2, is a single mode waveguide if the thickness d is smaller than $333\,nm$. Furthermore, when the thickness is smaller than approximately 240 nm, all TM-modes are cutoff. Since we only want one mode (the fundamental TE-mode) to propagate inside the waveguide, we chose the thickness a little lower than the limit, $200\,nm$ as a result.

2.4.1 Propagation Constant & Effective Refractive Index

After the thickness of the middle layer is chosen, all the parameters expect θ_1 are known. Plotting left hand side and right hand side of equation with respect to θ_1 separately, the value of θ_1 can be solved.

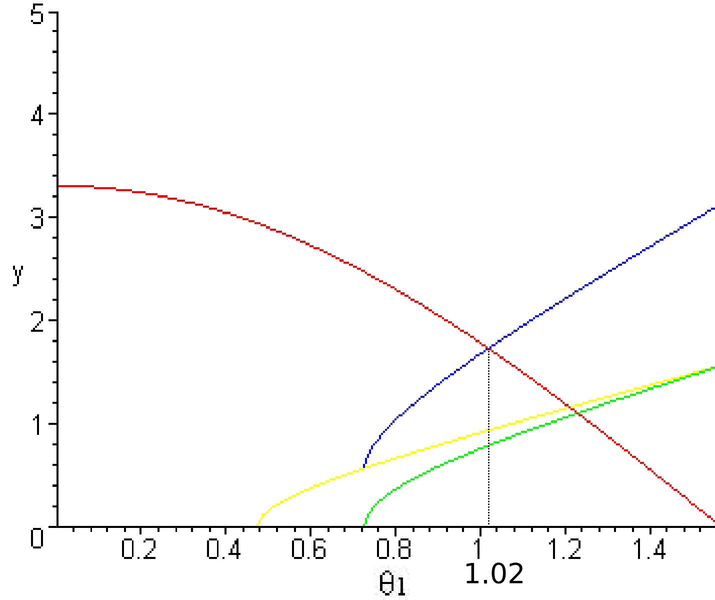

Figure 2.6: Graphical solution of equation (2.24) when $d = 200nm$ and $m = 0$. The red curve represents the left hand side of equation (2.24), whilst the blue one is the right hand side ($\phi_l + \phi_u$). The yellow and green one represents ϕ_l and ϕ_u separately.

According to figure. 2.6, the solution to equation (2.24) is $\theta_1 \approx 1.02(rad)$. So the propagation constant is

$$\beta = k_0 n_2 sin\theta_1 \approx 1.41 \times 10^7 \quad (2.29)$$

and the effective refractive index is

$$n_{eff} = \frac{\beta}{k_0} \approx 1.862 \quad (2.30)$$

Chapter 3

Characterization of Waveguides

This chapter is mainly focused on the characterization of the 2-D planar waveguide. Additionally, in section 3.4 and 3.5, two types of one dimensional waveguides are also characterized.

3.1 Designed Planar Waveguide Structure

We asked Dr. Gregory Pandraud from Delft University of Technology to make the waveguide for us. The designed structure of the waveguide is shown in Fig. 3.1. The nominal size of waveguide is 17.5 mm by 17.5 mm. Each waveguide consists of SiN, SiO_2 and Si layers from top to bottom, with nominal thicknesses of 200 nm, 2 um and 500 to 525 um respectively. The refractive indexes of SiN and SiO_2 layers are 2.187 and 1.453. Si layer, on the other hand, is not transparent at 830 nm. In the center of every waveguide, there is a free standing square SiN film, the width of which is labeled as a.

Dr. Pandraud made three wafers. Wafer #2 and wafer #3 is in Leiden while wafer #1 is kept in Delft. Each wafer has $4X4$ square elements (waveguides). Each wafer contains 4 groups (columns) of 4 elements, the width of which (indicated as a in Figure 3.1) increases stepwise from 100 um to 400 um, from column 1 to column 4 (see Fig 3.2). The size of the free standing films in the same column, however, does not change. The elements of the wafer are labeled as the elements of matrix: element ij refers to row i and column j. The width of the free standing film of element 11, for example, is 100 um and that of element 23 is 300 um.

3.2 Microscope Observation

We used a microscope with 10X, 20X interference objectives from Nikon, and a 50X objective from Olympus to inspect the profile of waveguides.

3.2.1 Calibration of optical microscope

In order to measure the size of the waveguide, calibration of different objectives has to be done first. The cutline between the elements are designed to be 160 um wide. Basing on the width of 160 um, we deduce the following calibration for the CCD camera connected to the microscope:

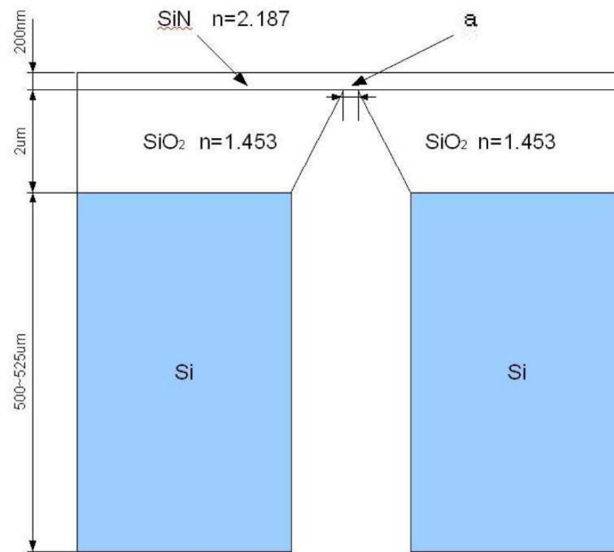

Figure 3.1: Side view of the waveguide consisting of SiN slab on top of SiO_2 layer, with the refractive index being 2.187, 1.453 *respectively. At the bottom, there is a Si substrate, being* 500 *um to* 525 *um thick.*

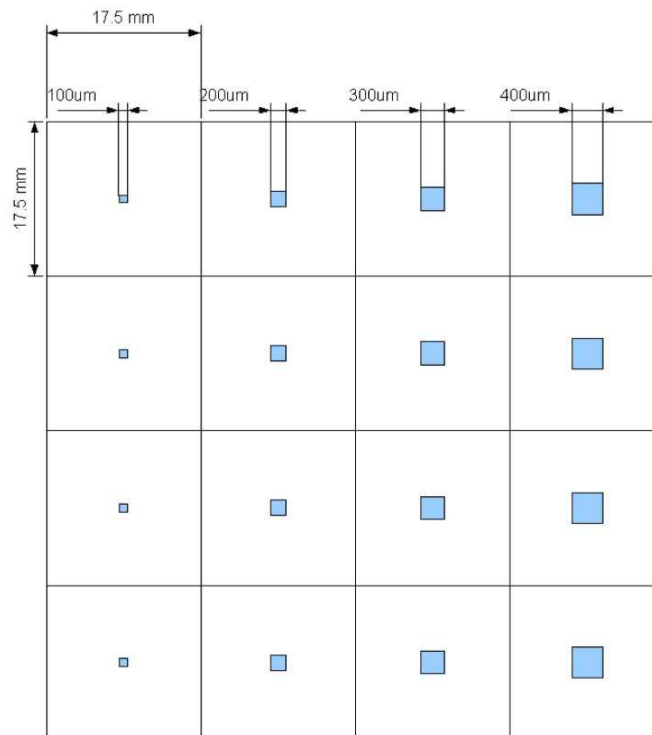

Figure 3.2: Top view of the whole wafer. The size of free standing film (shown as small squares in the middle of each element) increases stepwise from 100 *um to* 400 *um.*

10 X Objective

Firstly, we observed the cutline with 10 X objective and shot the image with the CCD camera attached to the microscope. (See Fig. 3.3) The dark area in Figure. 3.3 is the cutline. Measuring by the software MaxIm DL, we find that it occupies 312 $pixels$ horizontally. Hence the pixel size is $160/312 \approx 0.513$ $um/pxiel$

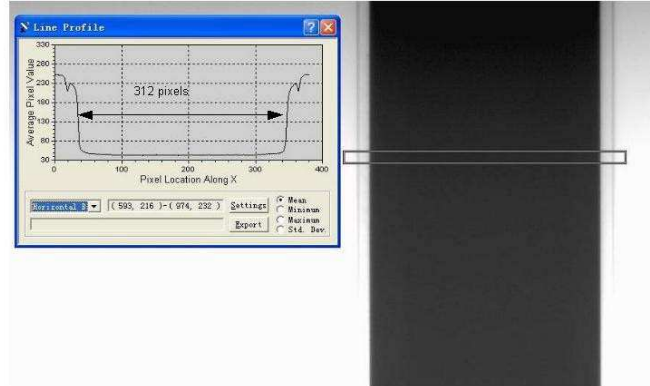

Figure 3.3: Image shot by camera associated with the microscope on 2008-12-10, and analyzed using MaxIm DL software. The dark belt is the cutline between elements.

Using the same idea, the pixel size under 20x and 50 X objective is obtained and shown below:

0.256 $um/pixel$ (20X interference objective)
0.090 $um/pixel$ (50X Olympus objective)

The 50X objective from Olympus works effectively as 57X in our Nikon microscope, being designed for a different tube length.

Optical inspection and size calculation

Fig. 3.4 and Fig. 3.5 shows the free standing SiN films of four typical elements from both wafer 2 and wafer 3, using 10 X objective. Basing on the calibration in section 3.2.1, the size of each is measured. It seems that the film is not perfectly horizontal, and the sizes of them are much different from the expected ones, namely, 100 um, 200 um, 300 um, 400 um. Some of the films look uniform, while other of them, however, have speckles on it. Conclusions are given on page 16

Wafer 2

The free standing SiN films on Element 11 to Element 14 on wafer 2 are shown in Fig.3.4 as a typical example and the size of each are also given in that figure. We find two squares in each picture. The inner one is the SiN film and the 20 to 25 um wide edges around it is the transition from a SiN-only film to a combined SiN-SiO_2 film with increasing SiO_2 thickness. The observed taper in thickness is remarkable. Both the size of inner square and the outer one is measured and denoted in Fig. 3.4

Wafer 3

Figure 3.5 shows four films in the second row (Element 21 to 24) of wafer 3. This time we find only one square with a very thin edge in each picture, which indicates the transition from the free standing

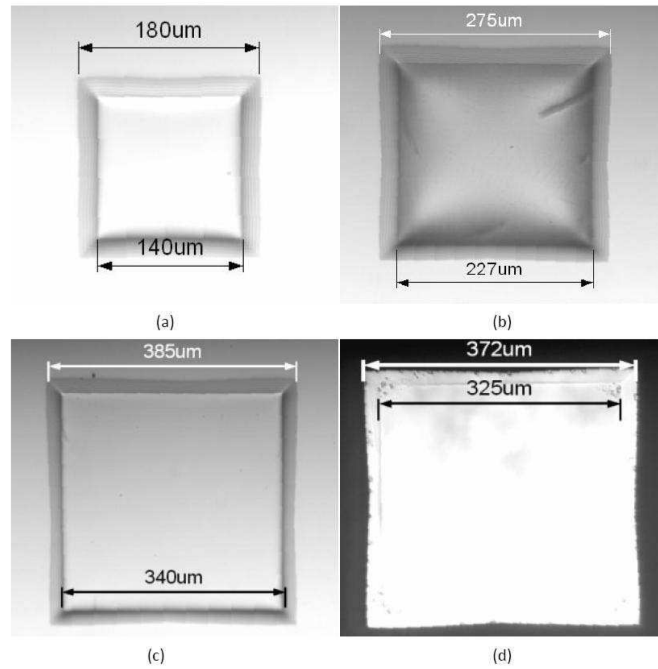

Figure 3.4: Optical inspection of wafer 2. (a) Element 11: the film looks very smooth and clean. (b) Element 12: several scars on the film. (c) Element 13: a smooth and clean film (d) Element 14 under a back illumination: many spots in the transition zone. The size of this film is comparable to that of element 13.

SiN film to the SiN-SiO_2-Si structure is very small. We find typically 2.5 um wide transition regions (see section 3.2.2). Similar sizes as that in Wafer 2 were found in Wafer 3.

Conclusion

1. The free-standing films on both wafers are around 140 um, 230 um, 330 um, 330 um from column 1 to column 4, instead of the designed 100 um, 200 um, 300 um, 400 um. The size of the films in column 4 is almost the same as that in column 3, both of them being around 330 um.
2. There is a noticeable difference between the two wafers in the transition from the free standing SiN film to full structure. The transition on wafer 3 is only about 2.5um wide and could hardly be seen with 10 X objective, while the transition is 20 to 25 um wide on wafer 2. The edge is believed to be the SiO_2 taper.
3. Generally speaking, most of the films on wafer 2 look cleaner than that on wafer 3. There are, however, a few exceptions.

3.2.2 Measurement of height profile

In this section we describe a measurement of the height profile of the free-standing films and the transition from these films to the full structure. For this purpose we used the 20 X interference objective from Nikon and 50 X objective from Olympus, applying both white light and monochromatic green light ($\lambda = 549$ nm) as illumination source.

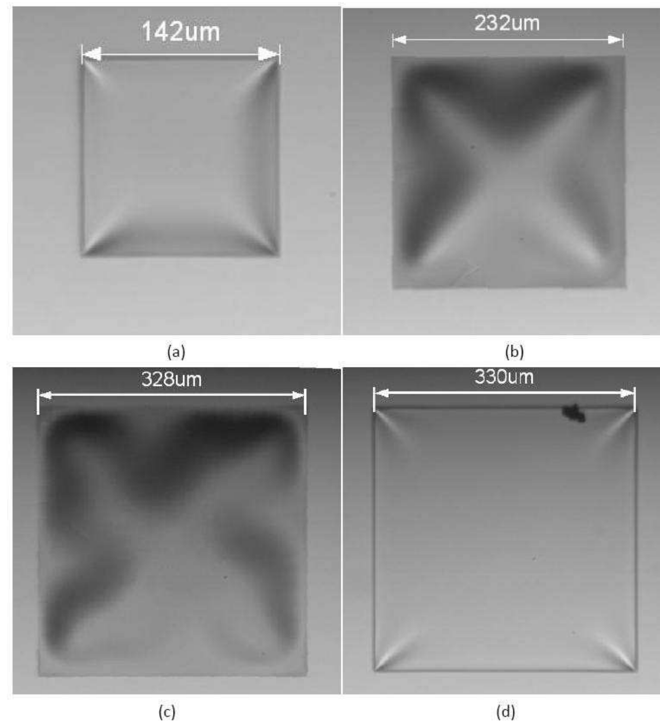

Figure 3.5: Optical inspection of wafer 3. (a) Element 21: the film looks clean. (b) Element 22: A big cross through the whole film is observed. (c) Element 23: this film is very similar to that of Element 22. (d) Element 24, there is only one defect near the top right angle. Again, the size is almost the same as that of Element 23.

Interference Objective

The interference objective is a variant of the Michelson Interferometer. Figure. 3.6 presents the basic arrangement of this kind of objective. The beam-splitting prism split the illumination light into two ways, one to the specimen and another to the reference mirror. There are two uniform objective lenses with completely identical optical distances in each of these two ways. The light reflected on the specimen goes through the prism and eyepiece and finally forms the image, while light reflected on the mirror is reflected again by the prism and goes through and finally generates the reflection image. If these two optical distances are the same, the interference pattern will come out.

Actually, the two uniform objective lenses are difficult to manufacture and the structure of the interference objective used in our group is a little different. (See Fig. 3.7) Instead of using beam splitter and two objective lenses, Nikon places a reflection reference mirror in the center of the objective lens, and interposes a half mirror between the objective lens and the specimen. So half of the light can go through the half mirror and focus on the sample, while the other half of the light is reflected to the reference mirror. These components are well arranged such that an interference pattern will appear if the system is focused on the specimen. If the specimen is tilted a little, interference fringes will appear because of the height difference between the sample and the objective. The two nearest interference fringes represent height changes by half a wavelength of the illumination source.

Height profile of free-standing film

According to the principle of interference objective explained above, the interference fringes give the height profile of the free-standing film. The height difference between two closest fringes is $\lambda/2 = 274.5$ nm for monochromatic light of $\lambda = 549$ nm.

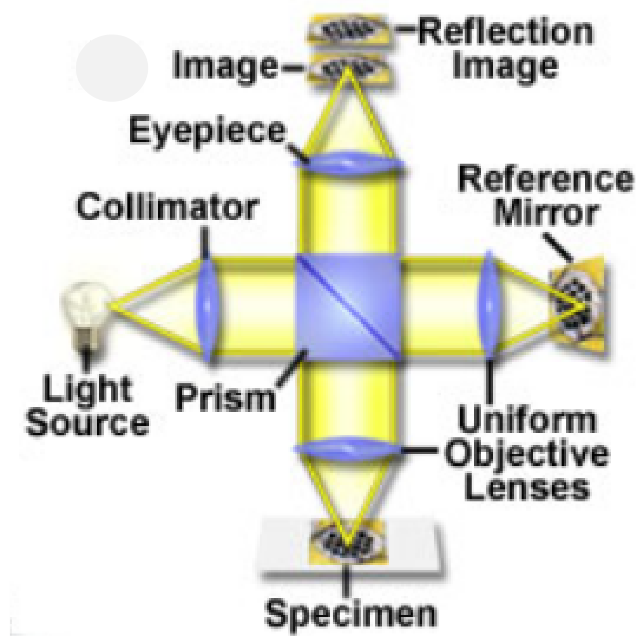

Figure 3.6: The principle arrangement of interference objective. (This picture is taken from the website of http://www.microscopyu.com/articles/interferometry/twobeam.html)

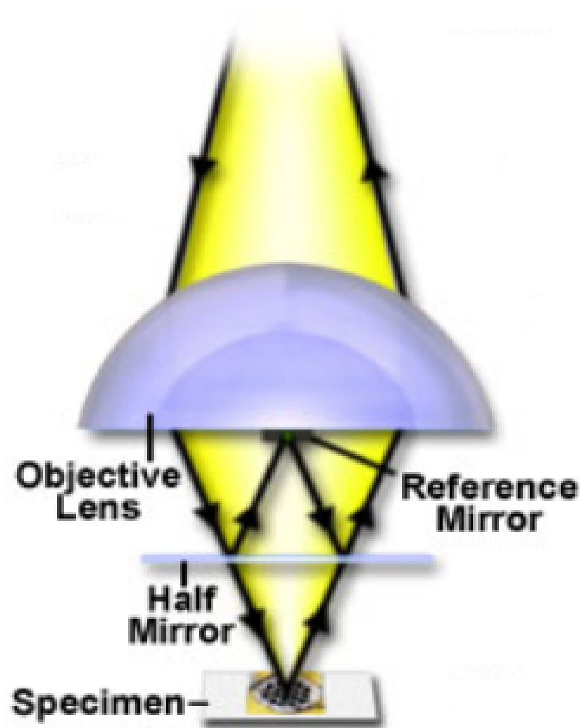

Figure 3.7: The real arrangement of interference objective from Nikon Corporation. (This picture is also taken from the website of http://www.microscopyu.com/articles/interferometry/twobeam.html)

The wafer is put on the stage a little downwards, so that the upper area of the images is a little higher than the lower. Fig.3.8 (a) is an image of Element 44, Wafer 2. The height profile along the black line of this film is roughly calculated and plotted in Fig.3.8 (b). From this figure we find that the middle part is approximately 1.2 *um* higher than the side. Fig 3.9 is another height profile image of Element 34, Wafer 3. Profile along the solid line and dashed line is different and shown in 3.9(b) and 3.9(c).

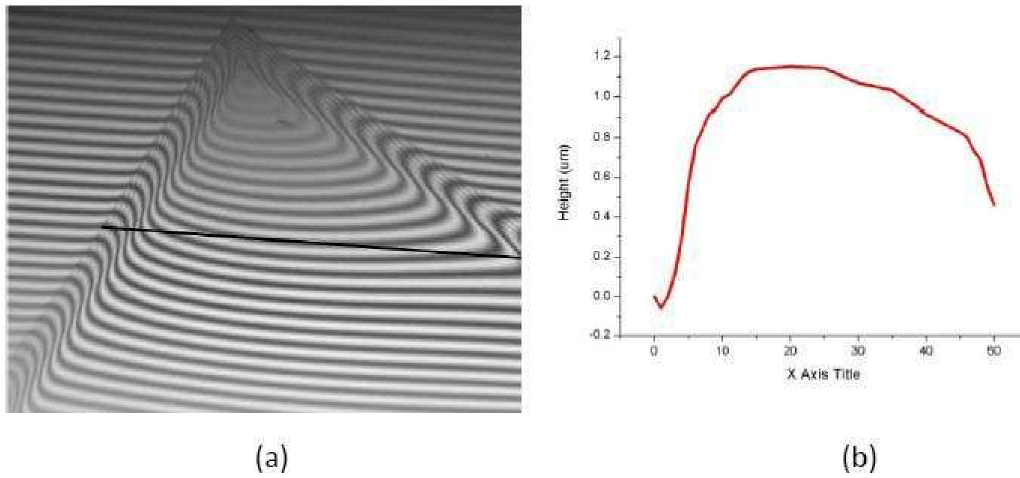

Figure 3.8: (a) Element 44, Wafer 2 observed with interference objective. (b) The height profile along the black line of (a). The dimension of the Y axis is millimeter, while the X axis is dimensionless.

Tables explaining all the height profile of free standing films on both wafers are shown on page 21 and 22.

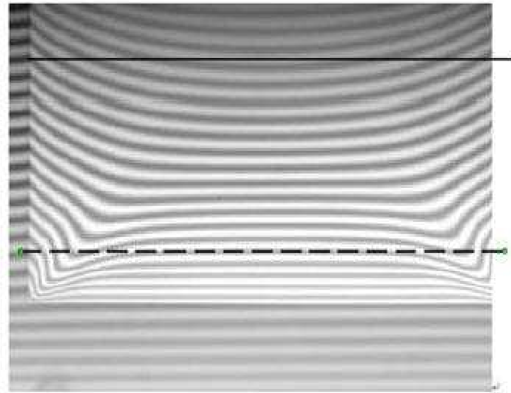

(a)

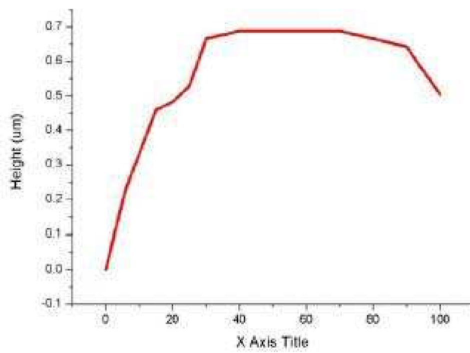

(b)

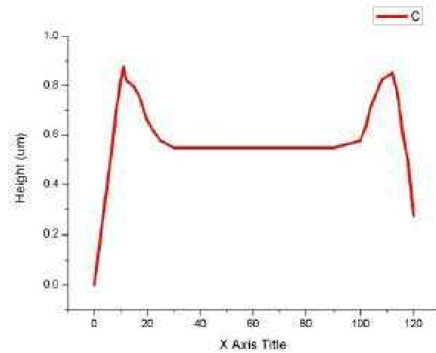

(c)

Figure 3.9: (*a*) *Element 34, Wafer 3: observed through interference objective.* (*b*) *Height profile along solid line, center is about 0.7 um higher than the side.* (*c*) *Height profile along dashed line is intriguing. Maximal value occurs at both sides.*

Summary of height contours of all 16 element of wafer 2

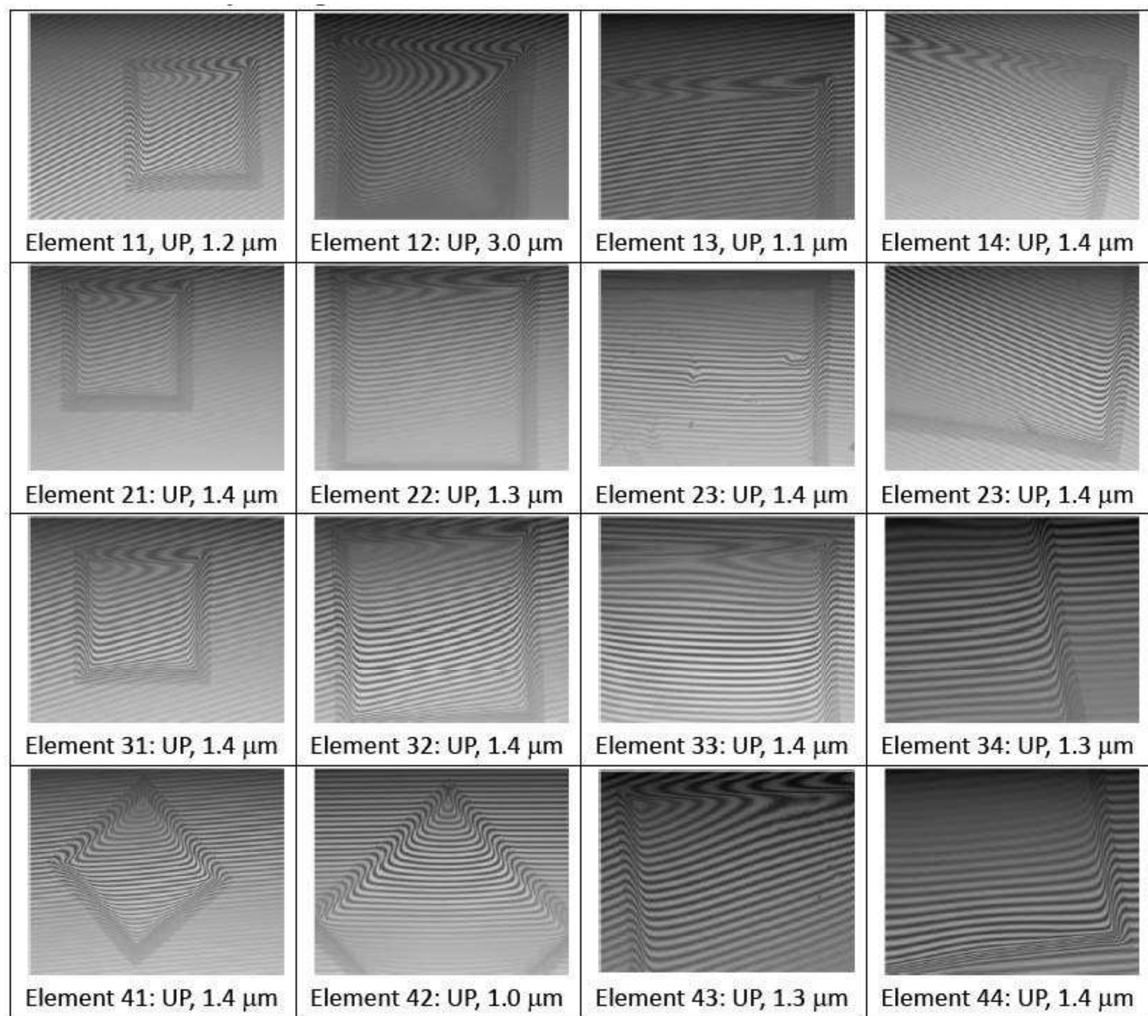

Conclusions:

- In wafer 2, all the free standing films bend up
- The typical height difference between the center and the side is 1.4 *um*, expect for element 12, which bends up by as much as 3.0 *um* instead.

Summary of height contours of all 16 element of wafer 3

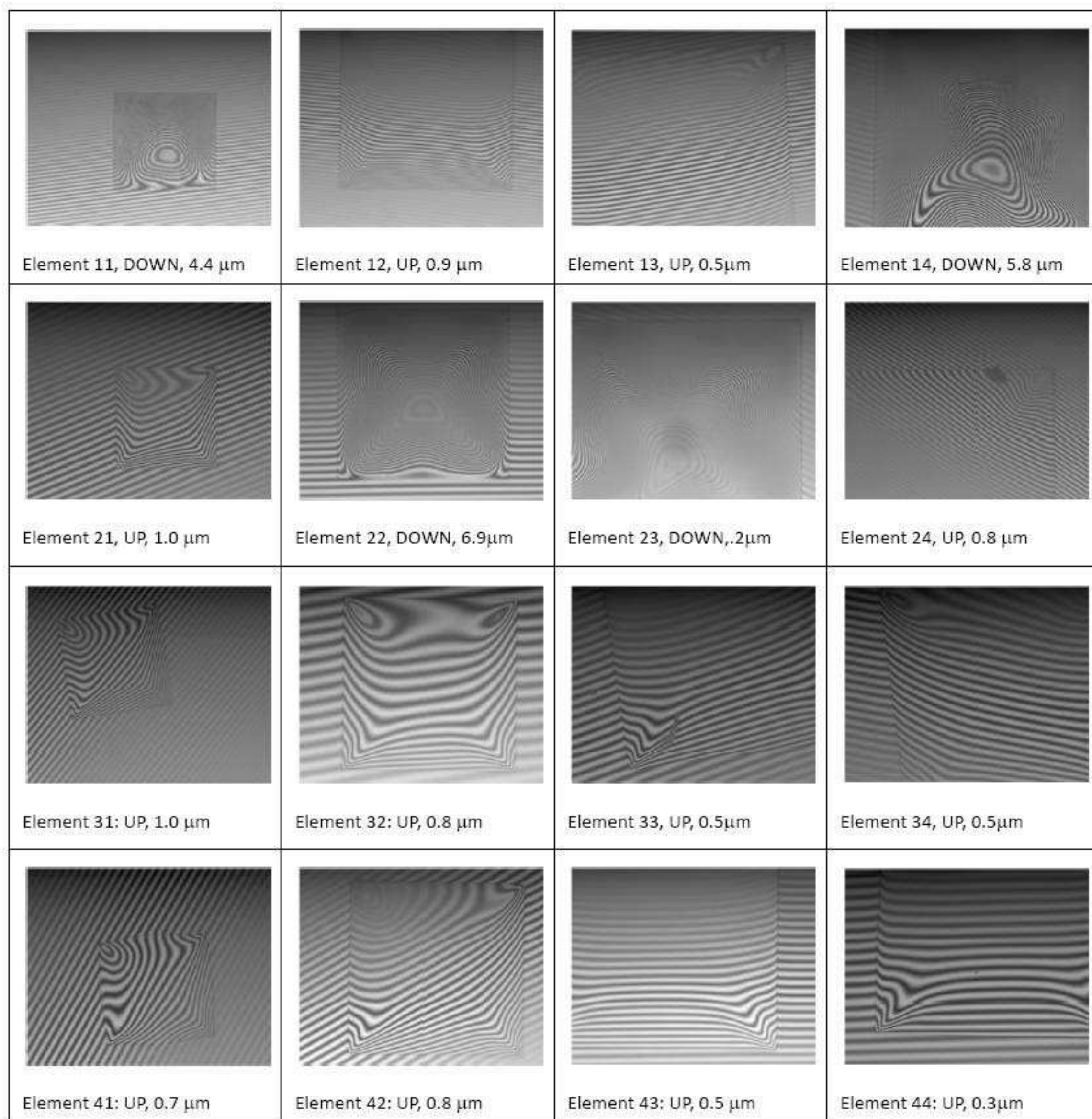

Conclusions:

- Films that bend upwards are generally smooth, whereas films that bend downwards get wrinkled
- Typical height for films that bend upwards is only about 0.5-1.0 *um*
- Typical height for films that bend down is much larger (4 to 10 *um*).

Optical coherence tomography

The thickness of the SiO_2 layer can be also measured with an interference microscope and white light (low coherence source), known as optical coherence tomography (OCT). The resulting picture shown as Fig. 3.10, shows one band of interference on the SiN film (lower part of the figure) and two bands in the full wafer structure (upper part of Fig. 3.10). These two bands correspond to optical reflection from either the top of SiN layer or the interface between the SiO_2 and silicon substrate. Using the spacing between these two bands, we find an optical thickness of 2.8 ± 0.2 um, corresponding to a physical thickness of 1.9 ± 0.2 um.

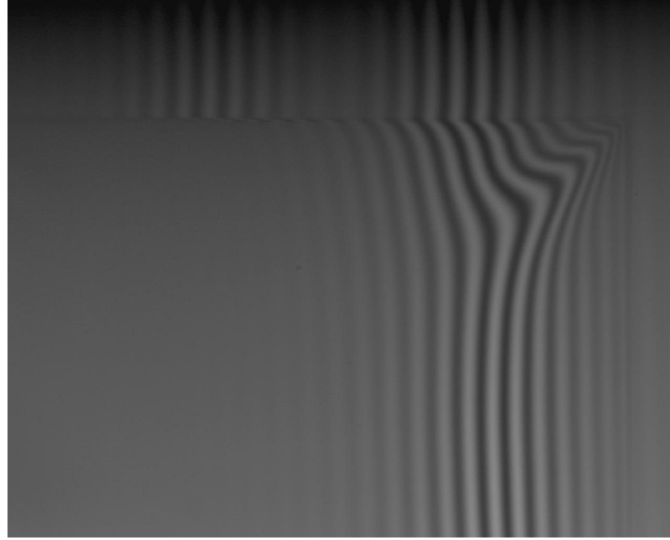

Figure 3.10: Two bands correspond to optical reflection from either the top of SiN layer or the interface between the SiO_2 and silicon substrate.

3.2.3 Facet observation

Observation with classical microscope

To check the side facet of a single chip we first use the 50 X objective lens. We observe two lines at the position where SiN and SiO_2 layers are supposed to be, one being sever times boarder than the other one. We expected that these two lines are the SiN and SiO_2 layers. However, the width of them as measured is about 0.5 um and 1.4 um respectively (See Fig. 3.11). We are clearly working at the resolution limit of the microscope.

Observation with electron microscope

To have a better observation of the side facets, which are produced by a combination of sawing and etching, a scanning electron microscope, $FEI\ NanoSEM$ 200, from the $BioAFM$ group is used. A single chip is mounted such that the surface normal of the facet under inspection makes an angle of 30 degree with respect to the e-beam (Sample is tilted 60 degree). In Fig. 3.12, to our surprised, 3 layers (different colors) instead of two 2 are observed, the height of which are about 189 nm, 735 nm and 4 um respectively, measured directly by the SEM itself. These thicknesses have been corrected for the observation angle, as indicated by the (cs) label in the figure. The 189 nm thick top layer might be an artifact arising from electric charging of the sample. Even if this is the case, we cannot explain the thicknesses of the other two layers, because the thickness of them should be 200 nm (SiN) and 2 um (SiO_2). Nevertheless, Fig 3.13 and 3.14, we could see that both the SiN and SiO2 layers do not look smooth. They both have some spots. The boundaries between these two layers and between the SiN

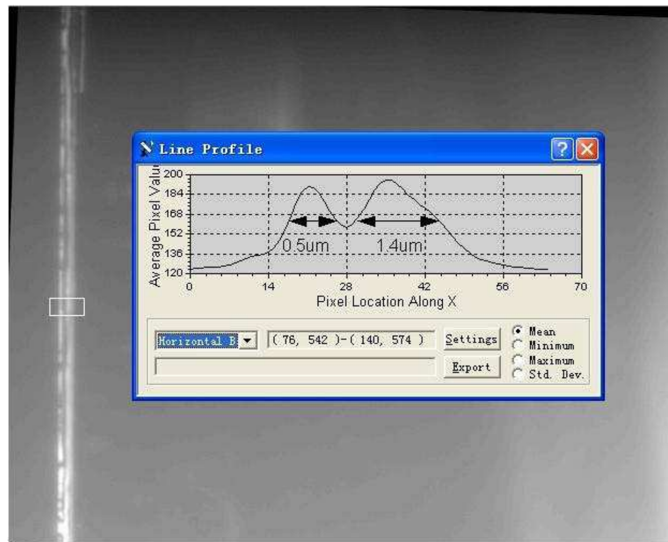

Figure 3.11: Optical inspection of facet of wafer with 50 X objective. Inset shows a horizontal cross-section over the indicated white boxed area.

and the air are not perfectly straight. For future observation with the SEM, it is advisable to admit water vapor to remove some of the charging effects.

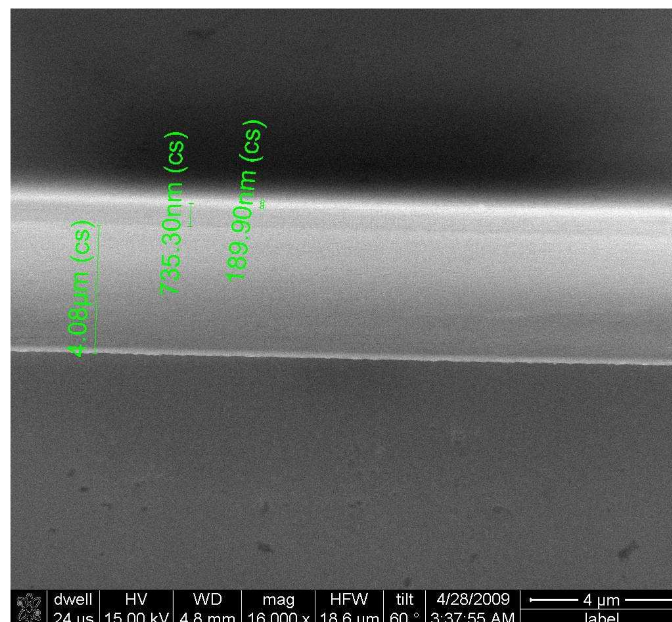

Figure 3.12: Three layers are observed with thicknesses of 190 nm, 735 nm and 4.1 um respectively. The SEM is working at $15kV$*, under high vacuum condition.*

3.3 Conclusions of 2-D Waveguide

Optical inspection of the top surface of the wafers with a microscope gave the following results:

1. The size of the free-standing film on both wafers is quite different from that is expected to be. For both wafers, we measure about 130, 230, 330 and 330 um instead of the expected 100, 200, 300, 400 um for the free-standing SiN-only film.
2. Most of the films on wafer 3 bend upwards by only about 0.5-1.0 um, while a few of them bend down sharply, with the typical height being 4 to 10 um. On the other hand, all the films on

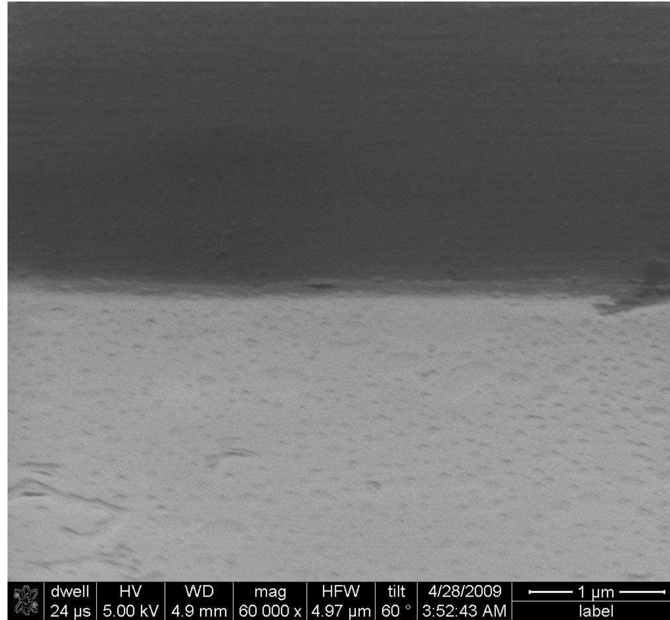

Figure 3.13: Image shot at the same working condition, but different location of the side facet. Notice the defect on the right.

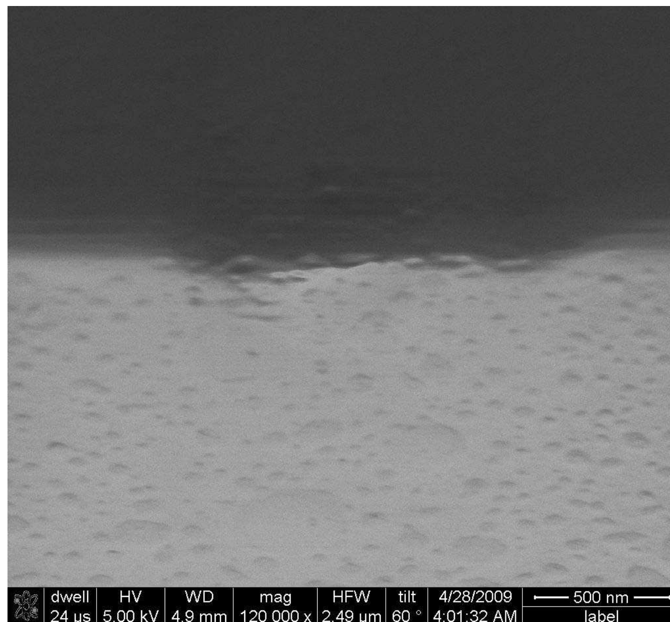

Figure 3.14: At some position, it seems the SiN layer is disappeared.

wafer 2 bend up by only about 1.4 *um*, expect one bends up by 3.0 *um*.

3. The taper-like transition on wafer 2 is about 20 to 25 *um* wide, while that on wafer 3 is only one tenth of that.
4. The films on wafer 2 are very clean and well designed, with only a few exceptions.

Inspection of the etched facets with a *SEM* (scanning electron microscope) showed:

5 To our surprise, we can distinguish three instead of two layers, although the top layer might be an artifact arising from electric charging. The measured thickness of the bottom two layers are much larger than expected: 0.74 and 4.1 *um* instead of the expected 0.2 *um* (*SiN*) and 2.0 *um* (SiO_2).

6 The surface of the facet is not perfectly flat but looks bumpy instead. The observed crater structure could probably result from the etching procedure or the incorrect handling separation method from wafer.

3.4 Characterization of 1-D Rib Waveguide

Because we do not very satisfy the quality of the waveguide, and because currently there are many researches on 1 dimensional waveguide[9][10][11], but few on 2-D planar waveguide, we ask Dr. Gregory Pandraud to produce new wafers for us.

3.4.1 Designed Waveguide Structure

The structure of new wafer is designed as below (See Fig. 3.15 and 3.16):

1. The new wafers are very similar to the old ones: the whole wafer contains 4x4 elements with dimensions of 17.5 x 17.5 *mm*. Layer structure of new wafer is identical to the old ones, being 200 *nm SiN* on 2000 *nm* SiO_2 on *Si* substrate; Size of the free-standing *SiN* film in the center of every element is 100 by 100 *um*, 200 by 200 *um* 300 by 300 *um*, 300 by 300 *um* from column 1 to column 4.
2. Instead of the 2-D slab waveguide, we now opted for 1-D rib waveguides [5]. The rib structure is produced by etching the rest part of the *SiN* layer further down by 50 *nm*. So the height of the rib structure is still 200 *nm* while the rest of the chip is 150 *nm* high.
3. The width of the rib structure w goes from 2 *um*, 5 *um*, 100 *um* to 2000 *um* from Row 1 to Row 4 of the wafer. The width of rib structure, w, does not change in the same row. In the top two rows, there are 3 pairs of ribs. The short distance between two ribs, indicated as d in Figure 3.15, is 50 *um*, and the distance between two pairs, dd, is 2 *mm*. The bottom two rows, contain 3 single lines, instead of 3 pairs, on each chip. The distance between two single ribs, dd, is still designed to be 2 *mm*.

3.4.2 Quality and Size Inspection

For the new rib type waveguide, under optical microscope with 10 X objective, the free-standing *SiN* film look much better than before. (See Fig. 3.17) The surface of the rib looks also perfect in this figure. On the other hand, we do detect some deadly defects in some waveguides. Three typical kinds of defect are shown in Fig. 3.18. The first one is related to the bad quality of the end face of waveguide, due to over etching of the sawing line. The coupling efficiency at this facet will be considerably low. The second defect looks like a scar across the whole rib structure. This defect will interrupt waveguiding because light propagating in the rib will all leak out from the scar. The third defect only happens on waveguides with large rib size (100 or 2000 *um*). Now only a part of the rib structure is

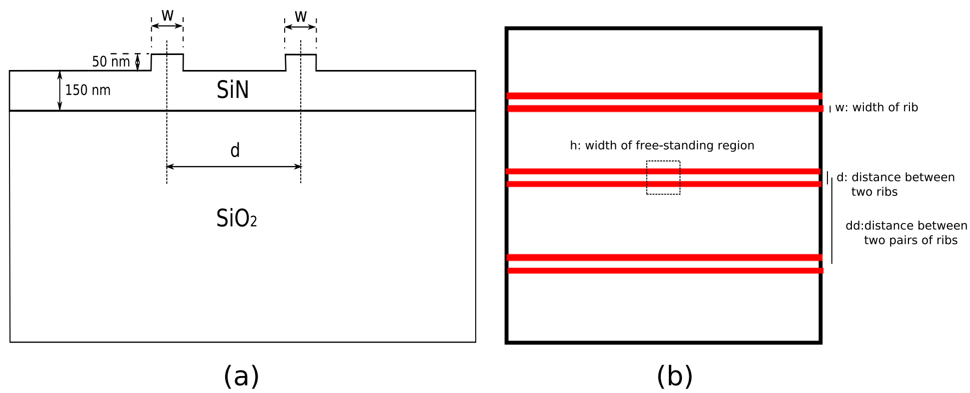

Figure 3.15: (a) Cross-section profile of 1-D waveguide. (b) Top view of one of the elements of the whole wafer. The red striplines represent the rib structures and the dashed square is the free-standing SiN region.

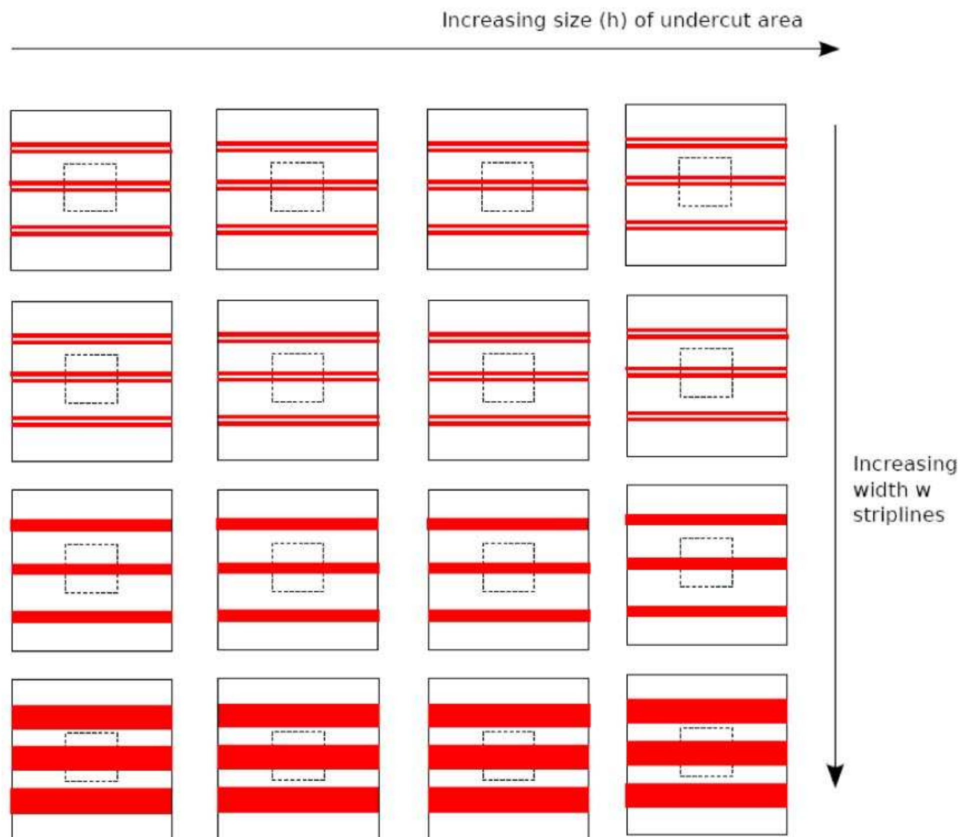

Figure 3.16: Structure of a whole wafer. There are 6 (3 fairs of) rib structures on every chips of the top two rows, while in bottom two rows, there are only 3 single ribs on every chip.

damaged by incorrect lithography process. Loss in this region is considerably large, but part of the light can still be guided to the end of waveguide.

So before trying to couple light into a waveguide, one should always inspect the quality of the waveguide using a microscope and choose the one with few and insignificant defects to ensure the coupling efficiency and to limit the loss.

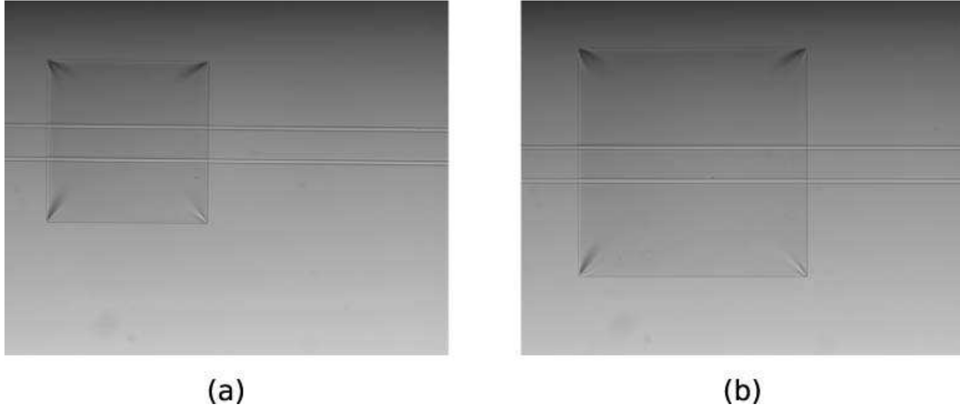

Figure 3.17: (a) Picture of Element 22 of a new wafer (UL1510 Wafer #4); (b) Picture of Element 23 of Wafer 4. From these two pictures we can see that the free-standing film is very clean and there is a sharp transition from the SiN only film to the full structure.

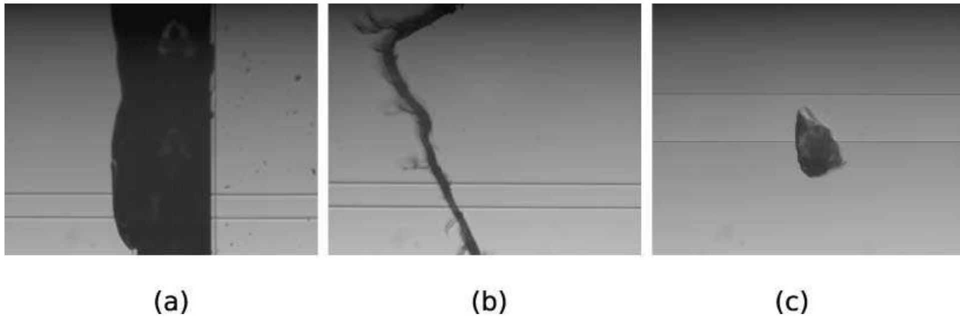

Figure 3.18: Three different defects in rib waveguides. (a) The cutline between two elements is not very straight, so the end face of the waveguide is not smooth. This will lead to a low in-coupling efficiency. (b) A large scar. Because this pair of ribs are cut, practically all light propagating inside the rib will leak out from the scar. (c) A big defect, which might result from the disruption of lithography, is shown on a 100 um wide rib structure. This size of this defect will also lead to a significant loss.

The rib width w and the distance between the rib pair d is measured by using the same method to measure the free-stand film discussed before. This time, because the rib is very narrow (several microns in the first two rows on Wafer 4), we use the 50 X from Olympus instead of the 10 X. Fig. 3.19 shows several pictures shot with the CCD camera attached to the microscope. Because the pixel size of this camera has already been calibrated (0.09 $um/pixel$ for 50 X Olympus objective), w and d can be measured by pixel counting. The thus measured value of w and d for different ribs is shown in Fig. 3.19. Generally speaking, it seems the larger the rib is, the more accurately it is produced (or measured). The 2 mm wide rib is too large to be measured even with the 10 X objective.

3.4.3 A noticeable structure at the end face

By observing the sawing line of the new wafer with the 20 X interference objective, we found a surprising structure.

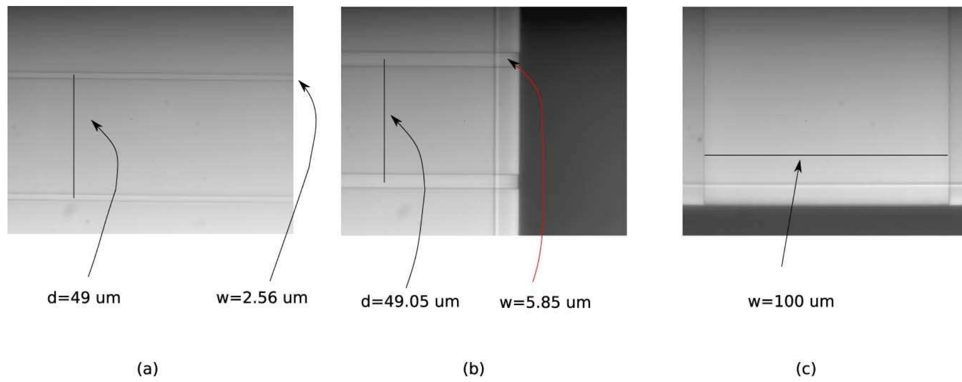

Figure 3.19: Waveguide structures observed with a 50 X objective. (a) Element 11 on Wafer 4. The measured width of the rib is 2.56 um instead of the designed 2 um, which is 28% wider. But the distance between the two ribs in the same pair is 49 um, which is very closed to the designed distance–50 um. (b) Element 21 on Wafer 4. The width of the rib is 5.85 um rather than 5 um (17% wider) and the distance d is almost the same as that in (a). (c) Element 31 on Wafer 4. Instead of a pair of ribs, a single one is produced, and the width is exactly as designed.

We put the sample under the objective such that the top right part of the waveguide in the image is higher the bottom left part. By using 20 X interference objective and monochromatic light source ($\lambda = 549\,nm$), interference fringes appear in Fig. 3.20. The wide dark belt is the sawing line between two elements on a wafer. From this figure, we can see that the fringes bend to a lower height on both side of the sawing line, which means that the edge of the element (waveguide) bends up a little. Drawing a line parallel to the fringes in Fig. 3.20, it is easy to find that the fringes bend only about one third of the distance between two fringe lines. So the edge of waveguide bends up by about 100 nm.

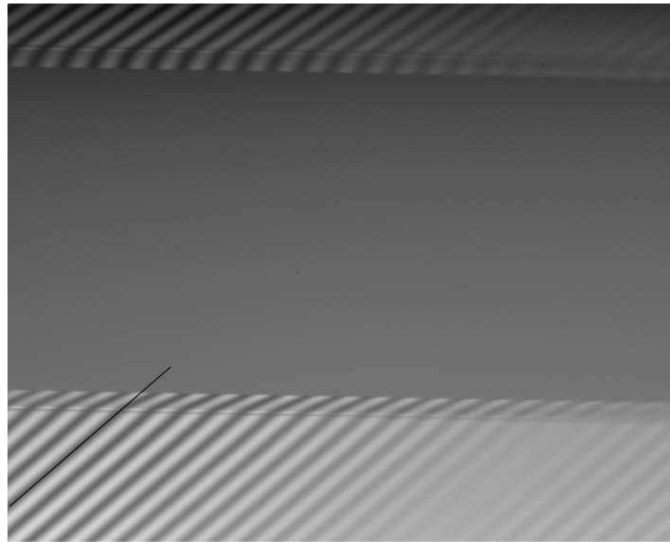

Figure 3.20: Sawing line between two elements of a large wafer observed with 20 X interference objective.

Actually, we saw this kind of phenomena before when we inspected the 2-D waveguide, but we thought the edge just bends down because of over etch; instead it probably also bends up. Actually we could not find any explanation for this structure until we discussed about it with Dr. Pandraud. He said that he used KOH to cut the sawing line (wet etching). This kind of etching methods is not 100% anisotropic, and the SiN is much less sensitive to KOH than SiO_2, so on each side of every element, there is also a free standing SiN part, just like in the middle (See Fig. 3.21). When etching is in progress, the KOH solution will fill in the space, where SiO_2 is removed, and generate a pressure upwards. This force pushes the SiN film up at the edge.

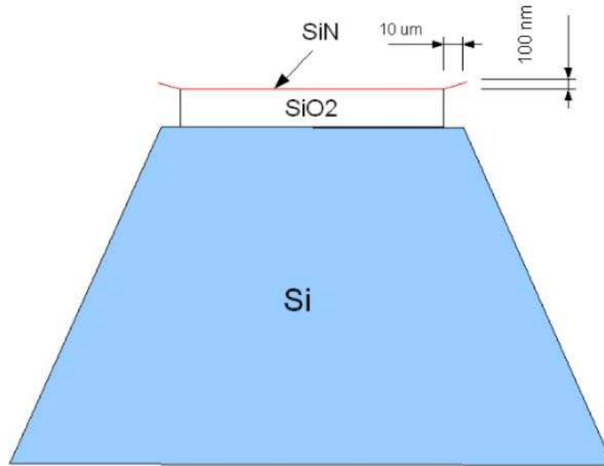

Figure 3.21: The correct structure of the waveguide.

Because the wet etching method produces the unexpected structure at the end face, it would be better if dry etching method, which is almost completely anisotropic, can be used next time.

3.5 The Test Waveguide

The third and final waveguide that we tested was designed by Gregory Pandraud as well. He operates this kind of waveguides successfully, using butt-end coupling with a fiber at an optical wavelength of 1300 *nm*. This is also a rib type waveguide (See Fig. 3.22). The rib is 4 *um* wide and 2 *um* thick, while the slab part beside it is 1.6 *um* thick. The guiding material is SiC, which has a refractive index of about 2.4 at 800 *nm*. The lower-cladding layer is 1 *um* SiO_2, and the upper-cladding is still air.

Since this waveguide is just a fragment from Gregory, broken off for testing purposes only, the quality of it is not great (See Fig. 3.23). Therefore, it is quite lossy.

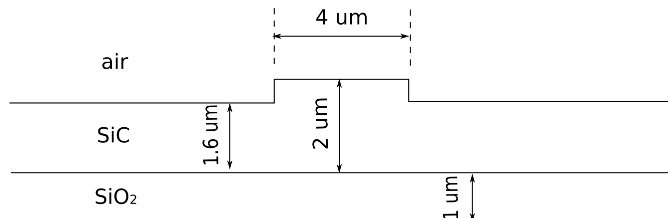

Figure 3.22: Sketched structure of Gregory's waveguide.

3.5.1 Measurement of stepwise height variation

It is difficult to measure the height of the rib with respect to the slab part with interference objective and green light, because this height does not change continuously. So the interference fringes shift discontinuously from slab to rib and we do not know which fringe on the rib corresponds to which line on the slab. Therefore, we can not use the method we used before to calculated the height difference. However, the low-coherence interference method can be used.

By using the white light source, the interference fringes are only visible over a small region with little height difference, and the darkness for each line is different. So we can say that the same darkness

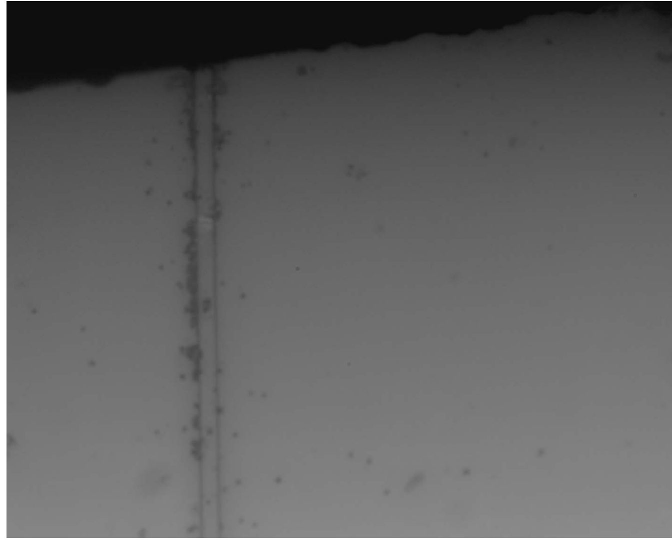

Figure 3.23: Microscope image of Gregory's waveguide inspected with 50 X objective.

refers to the same line. So I measure where the darkest line on the rib (878) and (893) is, and where the line close to the darkest one on the slab (873) is. The darkest line has thus shifted by $(\frac{893-878}{893-873}) = 0.75$ of a fringe. I put the sample such that the right side is higher than the left side. So the rib structure is higher than the slab, as expected. To calculated the height difference, we need to know the effective wavelength. In an earlier experiment we determined this effective wavelength to be 582 nm, so the height difference is $\frac{582}{2} \times \frac{3}{4} = 218\,nm$. It is only a little larger than half of the etched depth that Gregory mentioned!

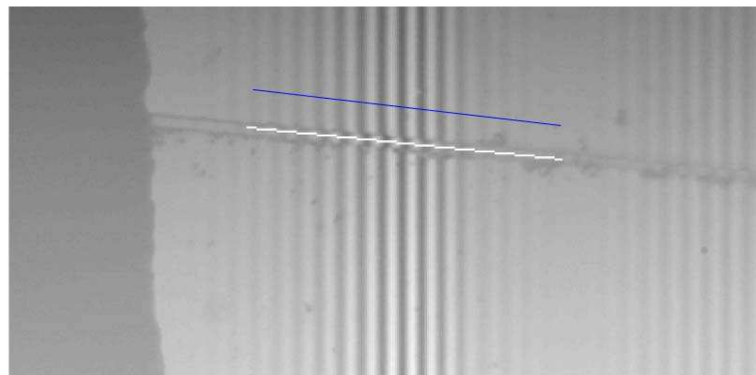

(a)

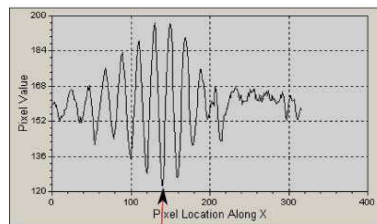

(b)

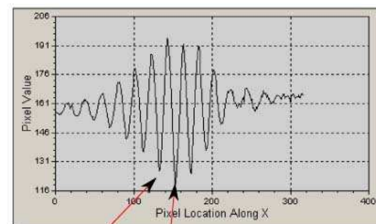

(c)

Figure 3.24: (a) Interference pattern of test waveguide under white light illumination, (b) Intensity profile along the white line in (a), (c) Intensity profile along the blue line in (a). Two groups of interference lines appear in this figure, just as in Fig. 3.10. One of them is due to the reflection between the interface of air and SiC, while the other one is because of the reflection between the interface of SiO_2 *and the subtract.*

Chapter 4

Experiments on in- and out-coupling for waveguides

4.1 Coupling Methods

Generally speaking, there are four kinds of methods to couple light to an integrated optical circuit, say, waveguide: prism coupling, grating coupling, butt coupling and end-fire coupling. (See Fig. 4.1).

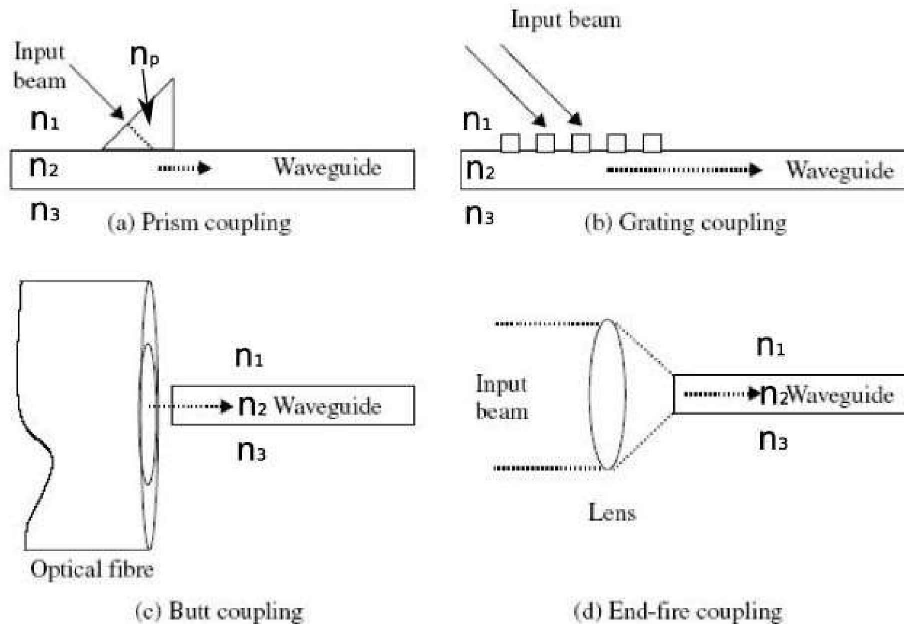

Figure 4.1: Four methods for coupling light to optical waveguide.

Prism coupling method has been demonstrated and calculated since several decades ago [6][7]. The principle of this method is that the z component of the propagation constant of light in the prism should be equal to the propagation constant β in the waveguide , which is referred to the phase match condition. Assume the angle between the beam and the bottom of the prism is α, then $k_0 n_p cos\alpha = \beta$. So the refractive index of the prism n_p should be larger than n_2 (See Fig. 4.1a). The coupling strength between the prism and the waveguide, the size of the incoupling beam and its position with respect to the prism's edge also matter.

Grating coupling should also fulfill phase match condition. But this time, the mismatch between the propagation constants in air and waveguide are matched by modulation with periodic gratings.

Assume the period of the grating is Λ, if the propagation constant can be modulated such that

$$\beta - \frac{2m\pi}{\Lambda} = k_0 n_1 cos\alpha. \tag{4.1}$$

the incident beam will be coupled into the waveguide.

The principle of Butt coupling and end-fire coupling is the same: try to make the incident beam on the end face of the waveguide as small as possible or even better try to match the size and shape of the waveguide mode. For butt coupling, people move a extremely narrow fiber very close to the end face of the waveguide to get a tiny spot, while for end-fire coupling a light beam is focused simply by lens on the facet of waveguide. The coupling efficiency depends on several factors.

Firstly, it depends on the overlap of the incident beam and the guided mode profile. As Fig 4.2 indicated, the incident beam (normally a Gaussian beam) is quite large compared to the size of the waveguide, which is the exact situation of my project, and only a small part of the beam can be guided into the waveguide because of the limited overlap between the Gaussian and the guided mode.

Secondly, coupling efficiency depends on the reflection from the waveguide facet. According to Fresnel equations, when light beam travels from the low refractive index material to the higher index material, a significant fraction of the incident beam will be reflected. The more the power reflected, the less the light beam coupled in.

The third main factor is the quality of the waveguide facet. The facet of the waveguide should be very smooth and clean to ensure that a large part of the light can go through the interface between the air and waveguide.

The fourth factor is the alignment of the optical system. Because usually the size of the waveguide is very small (at the order of 1 um or even less) the aliment between the incident beam and the waveguide is very important.

4.2 In-coupling system

In this project I use end-fire coupling to couple light in. The optical system is aligned as in Fig. 4.3. Because the numerical aperture of the waveguide is very large (larger than 1), to make coupling efficiency as large as possible, we want a large focused angle. We also want a large working distance to enable the additional use of a cylinder lens. For these reason, we choose a aspheric lens with 20 mm focal length to both make the focused angle large and get rid of spherical aberration. I use four mirrors to expand the traveling distance of the laser beam in order to make its width large enough. Because we want the beam to be vertically focused on the end face of the waveguide and horizontally focused in the middle of the waveguide, i.e., the free-standing film region, we use a cylindrical lens with $-80\,mm$ focal length to expand the beam horizontally. The top view and side view of the optical system is shown in Figure.4.4. Using a combination the aspheric lens and cylindrical lens like this, the beam will be a horizontal line on the front facet of the waveguide.

4.2.1 Measurement of focus size

According to the first factor of the coupling efficiency mentioned above, the incident beam on the end face of the waveguide should be as small as possible. So we have to check the size of the focus. The pixel size of the Laser Beam Profiler from Spiricon Corporation (called Spiricon for short) is 4.4 um, larger than the expected beam size at the focus point. So the beam profile cannot be detected by the

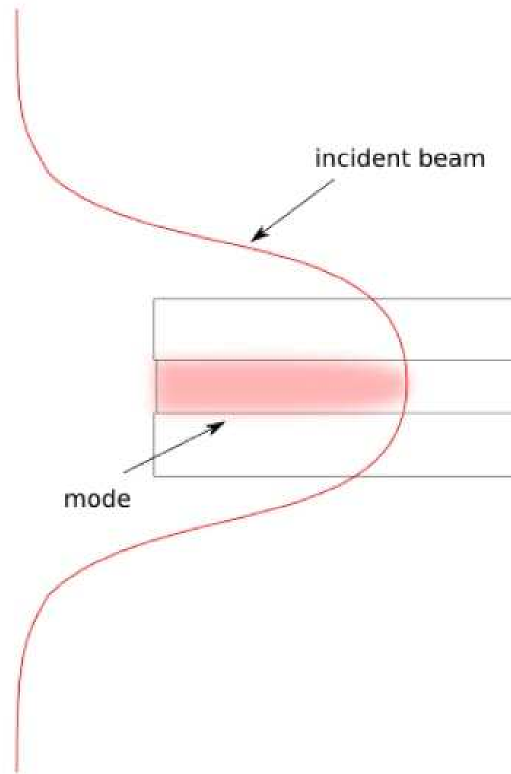

Figure 4.2: The overlap of the excitation Gaussian beam and the fundamental mode.

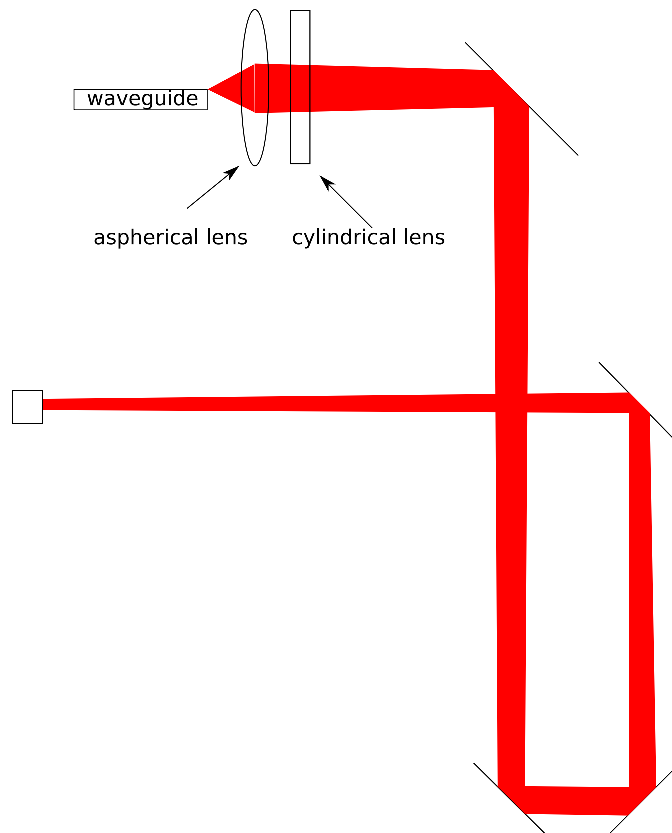

Figure 4.3: The in-coupling system.

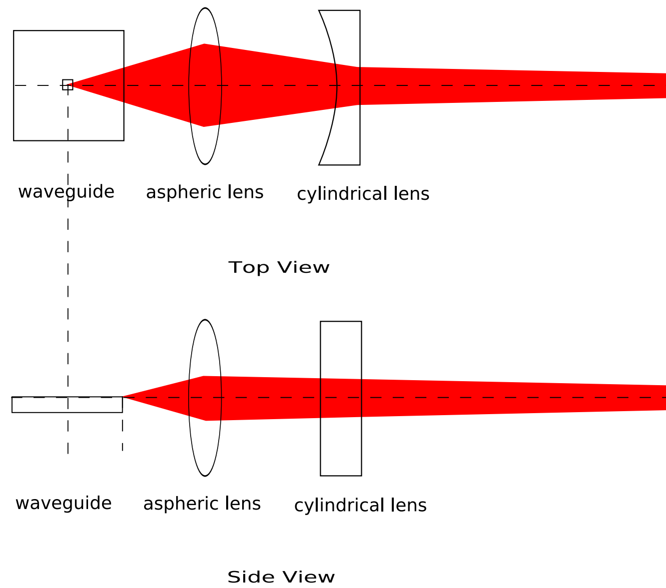

Figure 4.4: Top view and side view of the in-coupling system.

Spiricon directly. Thus, I use an objective lens to magnify and then measure the beam size. As Fig 4.5 shows, I first remove the waveguide from the focus point, and replace a 40 X objective lens a little behind the focus of the beam. Then I place the Spiricon behind the objective lens (15 to 20 *cm* from the objective). By adjusting the objective forward or backward such that a smallest beam profile is shown in the Spiricon, the focus of the beam can be magnify and imaged onto the Spiricon.

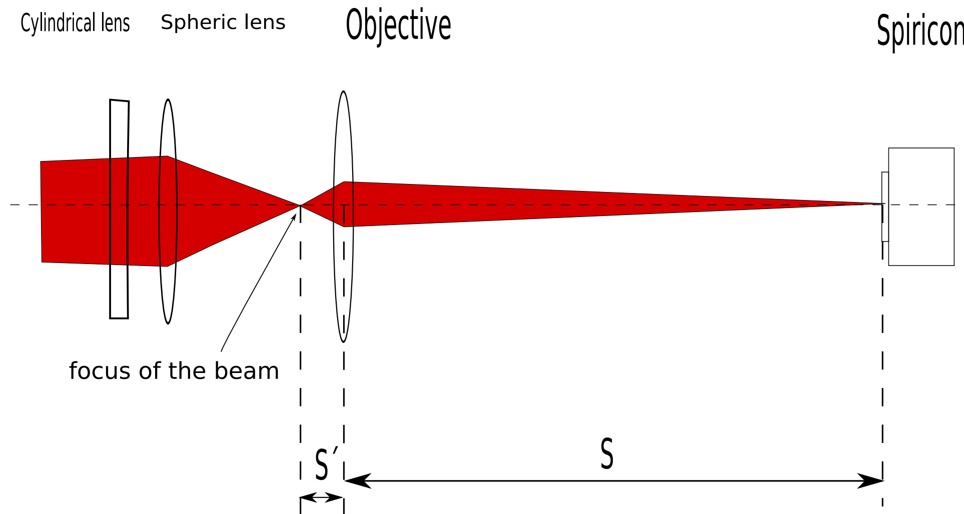

Figure 4.5: System for measuring the beam size at the focus.

Magnification of the objective lens

The distance from the focus of the beam to the optical center of the objective s' (object distance) and the distance from the optical center of the objective to the image s (image distance) obeys $\frac{1}{s} + \frac{1}{s'} = \frac{1}{f}$, where f is the focal length of the objective lens. And the magnification, in principle, is $M = s/s'$.

However, the magnification can not be calculated by measuring the distances from the object to lens and from lens to image for two reasons. Firstly, we do not know where the optical center of the objective is. Secondly, we do not know where the sensitive screen of the Spiricon is. However, the magnification can also be determined in a alternative way. The idea is shown in Fig. 4.6. I first move

the objective downward by h', so the optical axis of the objective (blue line) is moved down by h' from the optical axis of the combination of the lenses (green line). Because the pixel size of the Spiricon is known (4.4 um per pixel), the distance $l = h + h'$ of the image of F moves due to the displacement of the objective can be measured directly. The maginification $M = s/s' = h/h' = (l/h') - 1$. Accordingly, in our experiment, the magnification of the objective is measured as 42.5.

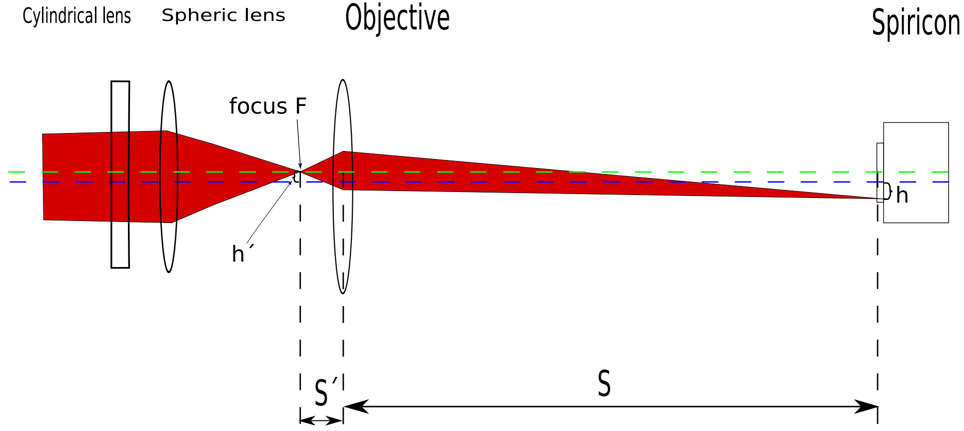

Figure 4.6: Measuring the magnification by moving the objective.

The focused beam profile

At first, only the asperical lens is mounted in the optical system. The magnified beam profile is measured by the Spiricon. By adjusting the objective lens along the optical axis, the minimum spot size is found (See Fig. 4.7(a)). Importing the data to Matlab, the full width at half maximum (FWHM) of the focus is measured and shown in Fig. 4.8(a). As the pixel size of the Spiricon is 4.4 $um/pixel$, the beam is approximately $\frac{13\times4.4}{42.5} = 1.35\,um$ at focus. Then the cylindrical lens is added to the system. Repeating the measurement, the beam profile is measured(Fig. 4.7(b)), and the FWHM of it (Fig. 4.8(b)) is calculated to be approximately 1.25 um. It seems the beam profile is better when the cylindrical lens is included, because the width of the beam at focus is slightly smaller. However, in Fig. 4.7(b) we can see that there are two small pedestals beside the center, which are absent in Fig. 4.8(a).

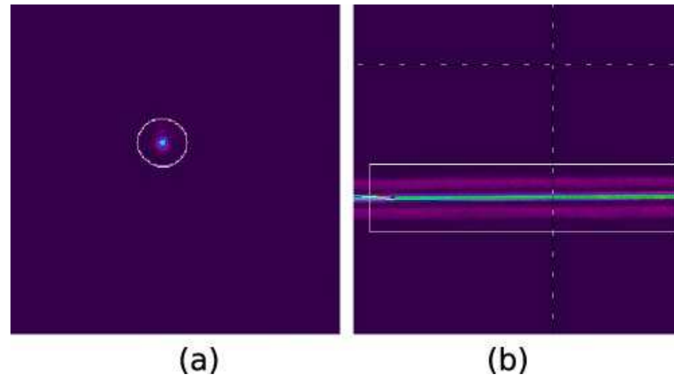

Figure 4.7: Beam profile measured by Spiricon in a false-color scale (a) circular spot behind aspherical lens, (b) strongly elongated foucs behind a combination of a cylindrical and aspheric lens.

Even now that we can make the beam size as small as 1.25 um, however, it is more than 6 times as large as the core layer of the waveguide, which means only a small fraction of the beam can be coupled into the waveguide.

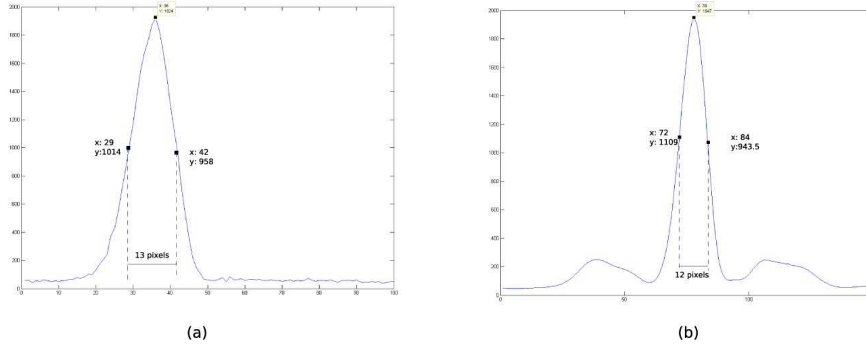

Figure 4.8: The FWHM of beam, (a) Behind aspherical only, (b) behind a combination of a cylindrical and aspheric lens.

4.2.2 Location of the Focus of the In-coupling Beam

From the above method, we know only that the focus of the beam can be modified as small as 1.3 *um*. However, we still need to know if the beam focus is at the front facet of the waveguide or not. In other word, we need to check if the beam size at the front facet is the smallest.

Our method of measuring the beam size at the front facet of waveguide is explained below. At first, the laser focus is positioned below the surface of the waveguide, so it is blocked by the waveguide and its holder. Thus, there is no light leaking over the waveguide and going to the power meter, which is put behind the waveguide to measure the power of this kind of leakage. If I keep moving the objective upwards by tuning the x adjuster of the Elliot stage with step length of one unit, the power measured with the power meter will increase because a larger and larger fraction of the light beam will leak to the power meter. If the beam size is large, I need to tune many units of adjuster x to unblock the whole beam, so the power changes slowly with displacement, and vice versa. So the steepest increasing of the power corresponds to the smallest beam size at the front facet of waveguide. By moving the objective lens along the optical axis (defined as z axis in the system), I can change the beam size at the facet. So a series of power-v.s.-x displacement curves are plotted. The steepest one corresponds the smallest beam size at front facet of waveguide. In Fig. 4.9 the violet curve is the steepest, so when we tune the z adjuster to unit 10, the beam is focused on the front facet.

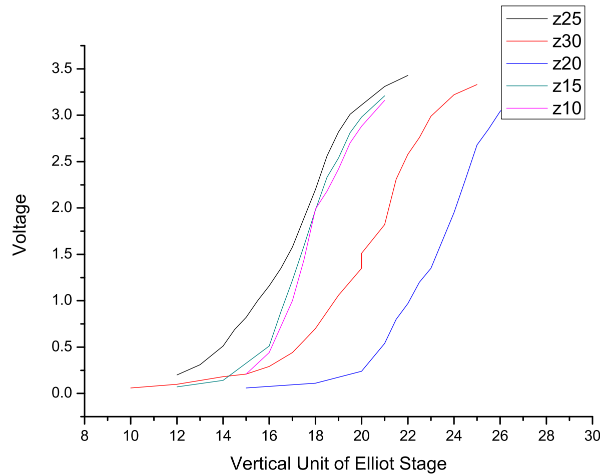

Figure 4.9: The leaked light power (expressed as a voltage) measured by power meter behind the waveguide with respect to x position of the objective (in vertical units of Elliot stage). Curves in different colors correspond to different position of z direction (also in units of Elliot stage)

4.3 Out-coupling system

To detect the out-coupling light from the waveguide, there should be a lens and a camera behind the waveguide. The lens we use is a standard $f = 50\,mm$ camera lens from Fujifilm Corporation. The camera lens has two advantages in this experiment. Firstly, the focal length of this camera is adjustable, so we can see both the front and back side of the waveguide without changing the position of this camera lens. Secondly, the field of view of the camera lens is so large that most part of back facet of the waveguide can be seen in one picture, and in this experiment we need a large field of view because we expect a bright long line coming out of the waveguide. The reason being that the waveguide confines the light only in the vertical direction. At top view of the expected propagation of the beam inside the waveguide is sketched in Fig. 4.10. The two yellow lines represents the horizontal width of the beam.

The camera we use in this experiment is Apogee Alta CCD camera from Apogee Instruments Inc. The pixel size of this camera is 9 um, and the exposure time can be adjusted from 10 milliseconds to 183 minutes. So it is powerful enough to detect weak intensity light.

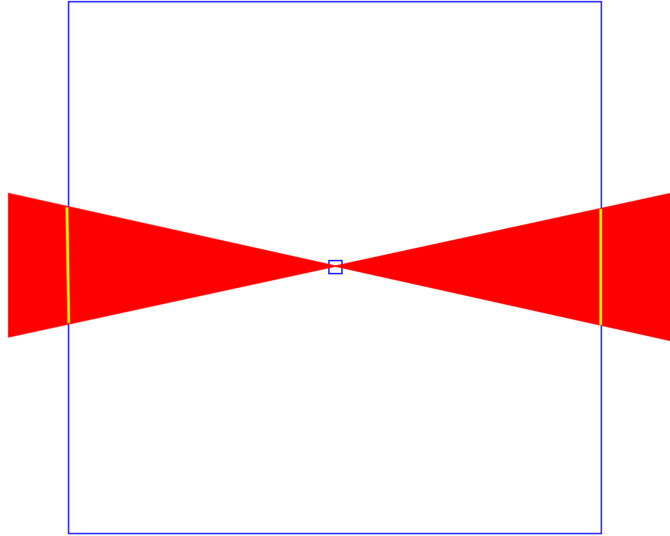

Figure 4.10: Top view of the beam propagation inside the waveguide. The large square is the waveguide and the small square is the free-standing SiN film where we want focus the light into.

4.4 Experiment result

4.4.1 Lloyd's mirror

The observation of light coupled into the optical waveguide is seriously hampered by the overwhelming presence of light leaking directly over the waveguide. Fig. 4.11 shows that this light exhibited a prominent striped interference pattern. We attribute this pattern to the well-known Lloyd's mirror phenomena. The surface of the waveguide, which is dielectric and smooth, serves as a mirror. When the cylindrical wavefront come from the in-coupling system (a combination of cylindrical lens and aspheric lens), is reflected by the surface of the waveguide and interferes with the direct beam. Then the dark and bright pattern appears depending on the difference of optical traveling length of these two beam (See Fig. 4.12).

Therefore, if this kind of interference pattern is observed, it means the focus of the beam is a little higher than the top of the waveguide. Furthermore, the higher the focus is, the more fringes can be

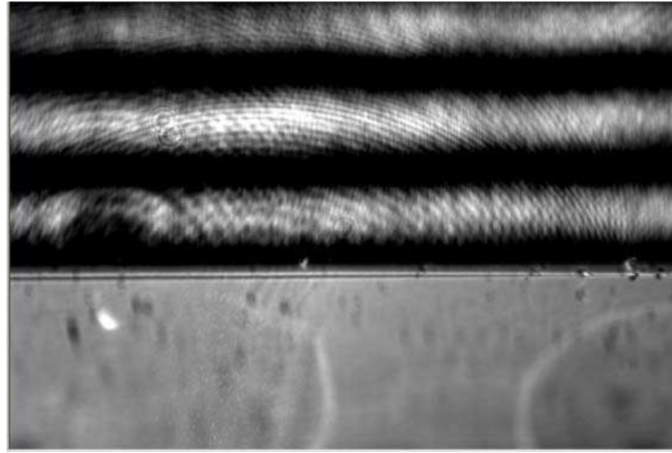

Figure 4.11: Fringes associated with lloyd's mirror phenomena. Light leaking over the waveguide displays interference observed with the Apogee camera. The lower part of this image is a waveguide.

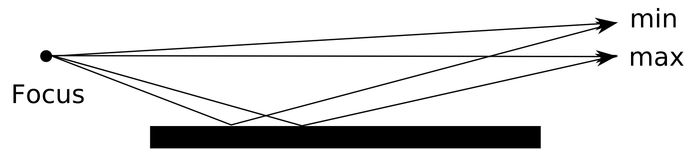

Figure 4.12: A sketched figure shows how Lloyd's mirror works

observed.

4.4.2 Tilted waveguide and razer blade

To separate the light coupling out of the waveguide and the light leaking over it, I tilt the waveguide such that the front side is 5.3 *mm* higher than the back side. Furthermore, I use a razer blade to block the light leaking over the waveguide (See Fig. 4.13). So in principle, only the light coupling out of the waveguide can be detected by the camera.

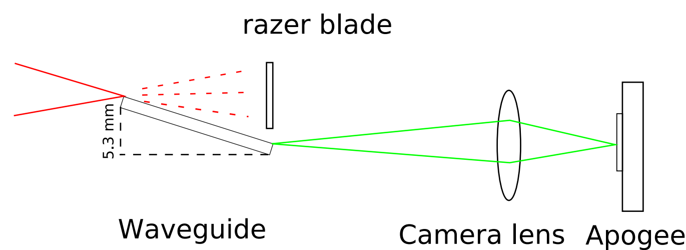

Figure 4.13: The waveguide is tilted such that the front side is higher than the back. Furthermore, a razer blade is used to block the light leaking over the waveguide.

4.5 conclusion

We have tried for several months to couple light into the many waveguides. Yet, we can not detect any light at the back facet of the waveguide that could be associated with in- and out-coupling. We can think of several limits to the in-coupling system which affect the coupling efficiency.

As I mentioned before, the smallest beam size which can be achieved is approximately 1.3 um, but the size of the waveguide is only one sixth of it. So the overlap between the focused Gaussian beam and the fundamental mode in the waveguide is very small. As a result, only a small fraction of the laser beam can be coupled in.

The stage, on which the in coupling system is mounted, is not so good to reach the required 200 nm precision. We mount the in-coupling system on a stage called Elliot Gold Series XYZ Flexure Stage from Elliot Scientific Corporation. They claim that the resolution of the adjusters is only 20 nm. We have calibrated that (the calibration will be explained in the next section), however, every unit of the fine tuning of the adjusters causes the displacement of 1.5 um. This is quite large compared with 200nm of the SiN layer.

Because the upper cladding is air, the surface of the waveguide should be extremely flat, otherwise losses will be very large.[8]

Last but not least, the facet of the waveguide is very ugly (Fig. 3.13 and 3.14), there is a free-standing SiN film bending slightly upward (Fig. 3.20 and 3.21) and we can not understand why the SEM picture Fig. 3.12 shows three layers with unexpected thicknesses.

4.6 Suggestions

Finally, I would like to suggest and promote prism coupling for 2-D planar waveguide in-coupling experiment. Prism coupling, as depicted in Fig 4.14, is a very good method for 2-D planar waveguide for several reasons.

1. Using this method, we do not need a perfect end face of the waveguide, because light beam is coupled from the top to the waveguide but not from the end face. And the same argument applies to out-coupling.
2. Using prism coupling, we do not need very good mechanics, because we do not need the focus of the beam to be exactly on the facet of the waveguide, and we do not need to adjust the height of the in-coupling beam and the waveguide to sub-micrometer accuracy.
3. Prism coupling allows for an easier separation between the light that couples into the waveguide and the rest of the incident light that does not make it. Under facet coupling, this spurious light travels along the wafer surface and easily reaches the imaging optics (Apogee Camera) of the researcher. Under prism coupling, this residual light will be reflected and will generally be well-separated from the in-coupled light not to bother the researcher again.

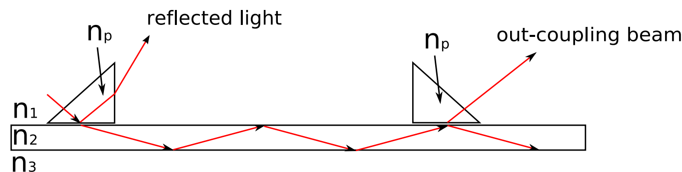

Figure 4.14: Sketched figure of the prism in- and out-coupling.

Chapter 5

Experiment on 1-dimensional waveguides

5.1 Complemental theory on rib waveguide

The rib waveguide, the structure of which is already shown as Fig. 3.22, is a waveguide that confines the light not only vertically, like a 2-D planar waveguide, but also horizontally in the rib section. This type of waveguide can be analyzed by the so called effective index method.

5.1.1 Effective index method

From the theory discussed in Chapter 2, the effective refractive index of the waveguide is introduced. According to equation (2.16) and (2.17) or equation (2.24) and (2.17), the effective index depends on the thickness of the waveguiding layer. For the same mode, the thicker the guiding layer, the large the n_{eff}. The effective index method comprises two steps. First the waveguide needs to be decomposed into the vertical and horizontal direction. We separate the waveguide to three sections from left to right, namely, slab section, rib section and again slab section (Fig. 5.1 (a)). Vertically, the effective index of the rib part $n_{eff,r}$ and that of the slab part $n_{eff,s}$ need to be calculated first. Because the thickness of the rib is larger than that of the slab,

$$n_{eff,r} > n_{eff,s} \tag{5.1}$$

In the top view of the rib waveguide (Fig. 5.1 (b)), it is clear that horizontally, rib section with the higher effective refractive index is sandwiched by the two slab sections with lower effective refractive index. So in the horizontal direction, it can also be regarded as a waveguide. So horizontally, the light can be guided inside the rib section but not leak to the other part because of total internal reflection.

5.1.2 Theory of single-mode rib waveguide with micron scale.

As calculated before, the core layer of the single mode waveguide should be at least 300 nm thick. The same is true for the one dimensional rib waveguide. However, according to Richard A. Soref et al, single-mode rib waveguide with large scale (several microns) is possible.[12] The authors mentioned that if the geometry of the rib waveguide is properly designed, higher-order modes will leak out of the the waveguide after propagating a very short distance, so only the fundamental mode will be confined inside the rib. As we know, the effective refractive index is smaller for higher order modes. So if the ratio of the thickness of the slab section to that of the rib section r is large enough, then the effective

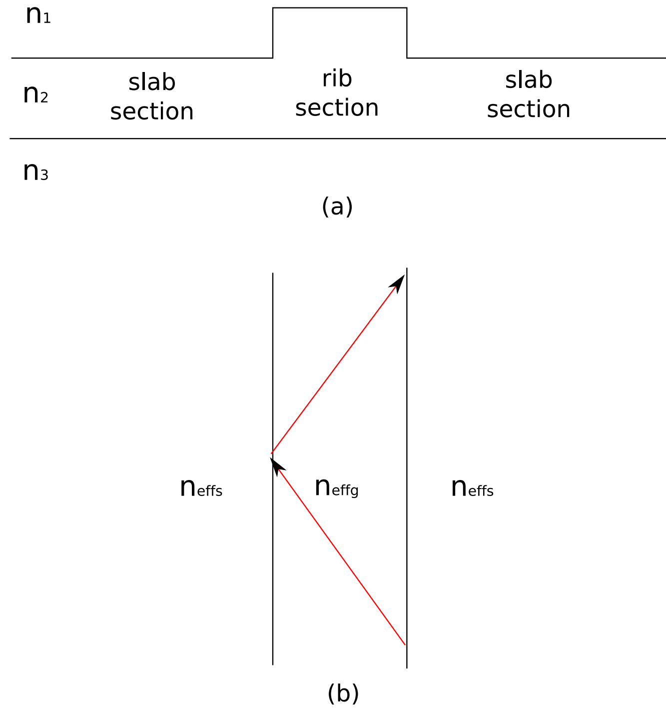

Figure 5.1: Sketched structure of a rib waveguide (a) Side view of the rib waveguide, (b) Top view of the rib waveguide. The light (indicated in red) propagates horizontally inside the rib section because of total internal reflection.

index of all the higher order of the vertical modes in the rib will be smaller than the fundamental mode in the slab. In that case the higher order mode will not be confined inside the rib anymore, but coupled to the fundamental mode in the slab part. In that paper the authors claimed that if the parameters in Fig. 5.2 fulfill the condition

$$\frac{a}{b} \leq 0.3 + \frac{r}{\sqrt{1-r^2}} \tag{5.2}$$

, after propagating several millimeters, there will be only the fundamental mode guided inside the rib. The higher order modes, however, leak to the slab part.

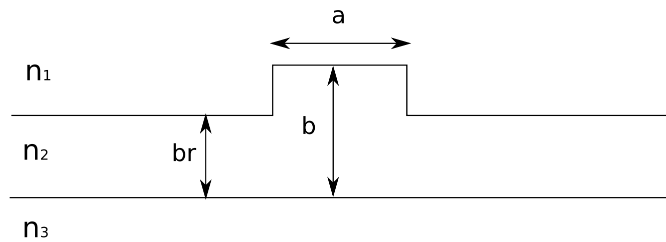

Figure 5.2: The structure of a rib waveguide with width a and thickness b. $r = a/b$ is the ratio of the thickness of the slab part to the rib part.

5.2 Optical system for rib waveguide

The coupling system that we will use for the rib waveguide is very different from that for planar waveguide (See Fig. 5.3). Instead of a combination of optical lenses and a camera lens for in-coupling and out-coupling system respectively, two 20 X objective lenses are used this time. And instead of the Spiricon, which is an outstanding camera for measuring beam size, a CCD camera called Apogee Alta from Apogee Instruments Inc is used. This camera is more powerful for imaging performance.

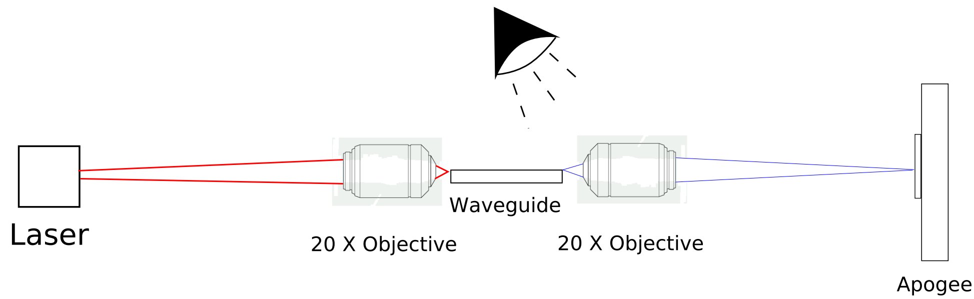

Figure 5.3: Optical system for 1 dimensional waveguide.

5.3 Detection of the Rib Structure

By shining an extra white illumination with an particular angle onto the waveguide (shown in Fig. 5.3), even 5 *um* wide and 0.5 *um* high structures can be detected by the out-coupling system (See Fig. 5.4 (a)). We found it somewhat surprising that the out-coupling system can detect a rib structure that is only 0.5 *um* higher than the other part. The pixel size of the Apogee CCD camera is 9 *um*, and even by using 20 x objective, it can only resolve $9/20 = 0.45\, um$ (the real magnification of the 20 X objective depends on the distance between it and the carema), so in principle, 0.5 *um* should only occupy one pixel and is hardly detectable. But on the other hand, the width of the bright short line and distance between the two lines fits the w and d of the waveguide very well. So we are convinced that the two bright lines are a pair of ribs.

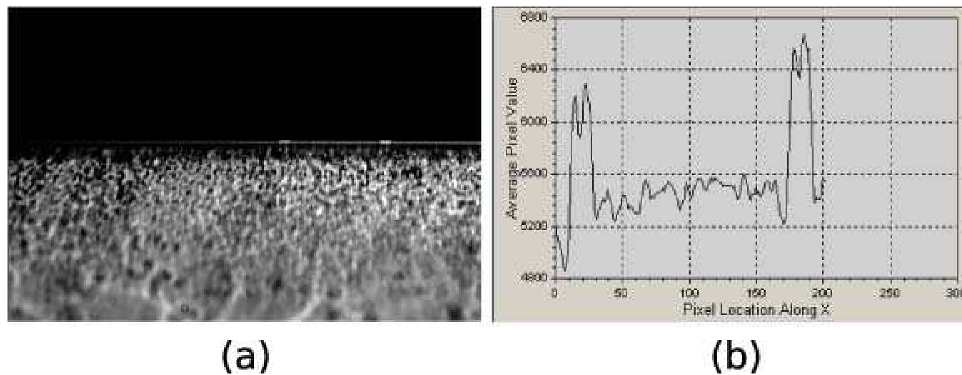

Figure 5.4: The 5 um wide rib structure is detectable by combining a 20 X objective and Apogee Alta camera. The width of the bright short line and distance between the two lines matches the width of the rib (5 um) and the distance between two ribs of the pair very well.

Actually, by measuring the distance between the two lines in Fig. 5.4 (a), the magnification of the 20 X objective can be calculated. Fig 5.4 (b) shows the intensity profile along the surface of the waveguide; the two peaks in this figure represents the locations of two ribs. The center of these two peaks are 164 pixels apart, corresponding to the distance 49 *um* measured by the optical microscope. So the magnified pixel size of the Apogee is $49/164 \approx 0.299\, um$. Thus the magnification of the 20 X objective in this optical system is equal to the pixel size of the Apogee camera divide by the magnified one, which is $9/0.299 \approx 30.12$. I indeed put the camera too far!

Each adjuster of the Elliot Gold Series XYZ Flexure Stage has a coarse tuning and a fine tuning. The unit size of coarse tuning can be measured by a vernier caliper. But that of the fine tuning, which is only the order of 1 *um*, can not be measured precisely in this way. However, using our imaging system, the fine tuning of the Elliot stage can be calibrated. Because the waveguide is mounted on the Elliot stage as well, moving the fine tuning by a few units already results in a significant displacement of the ribs in the image captured by Apogee. Since the magnified unit size is known, the displacement

of the ribs due to the adjustment of fine tuning can be calculated.

Fig. 5.5 (a) is the start point of this measurement. When I rotate the fine tuning of the y adjuster by 5 units, the ribs change their positions to that in Fig. 5.5 (b). Repeating this step 3 times, Fig. 5.5 (c), (d) and (e) are obtained. Fig. 5.5 (f) shows the horizontal intensity profile inside the small white rectangle of Fig. 5.5 (b). Since intensity profile of the same rib should not be changed by moving the whole sample, all intensity profiles of the right rib in different images have a minimum tip (pointed by arrow in Fig. 5.5 (f)), corresponding to the same position of the structure. Thus, by measuring how many pixels this tip moves, we can know the displacement because of the adjustment of the fine tuning. As a result, the unit size of the fine tuning can be calculated.

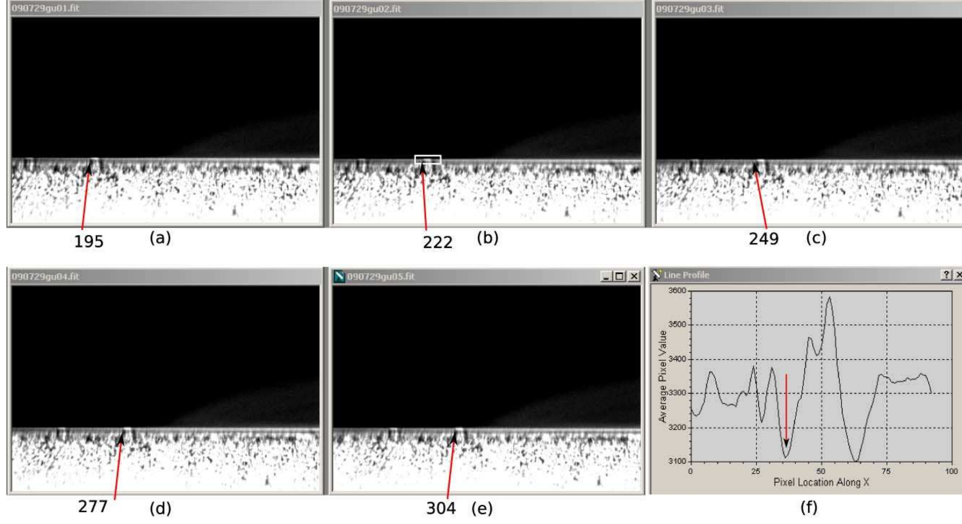

Figure 5.5: Calibration of y displacement of Elliot flexure stage. (a) The start point of this measurement, the pixel number of the left tip is 195. (b) This image is shot after rotating 5 units of fine tuning of y adjuster. The pixel number of the same position is 222. (c) Rotating 5 units more, the pixel number changing from 222 to 249. (d) Rotating another 5 units more, the first tip moves to pixel 277. (e) Rotating 5 units again, the left tip of the intensity profile of the right rib moves by another 27 pixels. (f) Horizontal intensity profile inside the while rectangle in (b)

Basing on Fig. 5.5, the rib moves 27 pixels due to a adjustment of 5 units. Since the pixel size of the image is 0.299 $um/pixel$, the unit size of the fine tuning is $\frac{27 \times 0.299}{5} = 1.61\,um$.

The fine tuning of x adjuster can also be calibrated in this way. According to Fig. 5.6, the rib now moves 24.4 pixels for every 5 units in average. So the unit size of the fine tuning of adjuster x is $\frac{24.4 \times 0.299}{5} \approx 1.46\,um$. The calibration in x direction is more reliable than that in y direction, because the sample could hardly be put perpendicularly to the 20 X objective lens.

The 100 um wide rib structure can also be detected by the CCD Apogee. In Fig. 5.7 (a), the structure inside the red dashed rectangle is related to the 100 um rib. The number of pixels it occupies is approximately 321 measured by the horizontal intensity profile inside the rectangle (Fig 5.7 (b)). So the width of rib measured by this optical system is $321 * 0.299 \approx 96\,um$, which fits the width of that rib well.

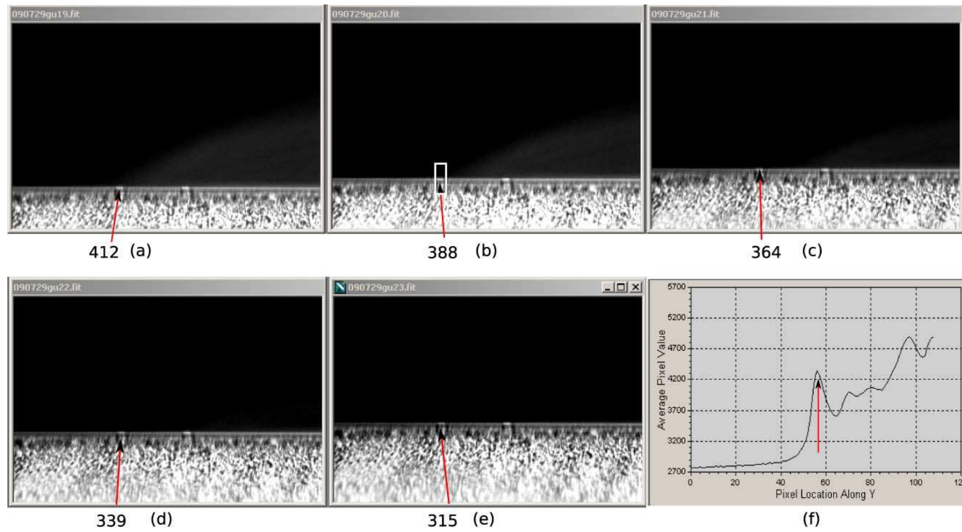

Figure 5.6: Calibration of x displacement of Elliot flexure stage. (a) The start point of this measurement, the pixel number of the left peak in vertical direction is 412. (b) After rotating 5 units of fine tuning of adjuster x, the left peak goes to pixel 388 in vertical direction. (c) Rotating 5 units more, the pixel number changing from 388 to 364. (d) Rotating another 5 units more, the first peak travels vertically to pixel 339. (e) Repeating that step, the first peak from left of the intensity profile moves by another 24 pixels. (f) Vertical intensity profile inside the while rectangle in (b).

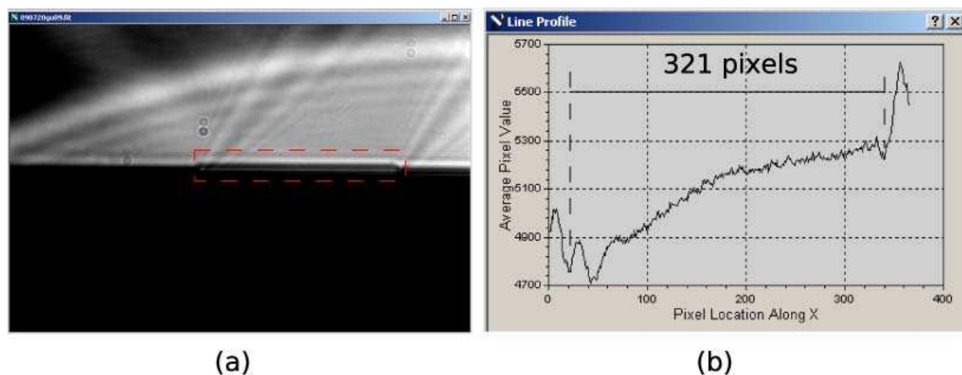

Figure 5.7: Image of 100 um wide ridge observed under the same illumination as Fig. 5.5. (a) The out-coupling objective is focused on the back facet of the waveguide. The structure inside the red dashed rectangle is believed to be the 100 um rib. (b) Horizontal intensity profile inside the red rectangle in (a).

5.4 Modified in-coupling system

In order to know if the focus of the beam is on the facet of the waveguide, we modified the system as shown in Fig. 5.8. Instead of letting the laser beam propagate directly to the in-coupling objective, we now put a 200 *mm* optical lens and a beam splitter in between. When the infrared laser is switched on, the laser beam is converged by the 200 *mm* lens first and finally hits the end face of the waveguide. Laser beam reflected by the facet of the waveguide is reflected again by the beam splitter (indicated in green in Fig. 5.8) and detected by a camera. We put the camera such that the distance between it and the beam splitter (L_2) is equal to distance between the focus of the infrared beam and the beam splitter (L_1). The reflected beam size detected by this camera changes when the objective is moved along its optical axis. When the smallest size is detected, we can say that the laser beam is focus on the waveguide.

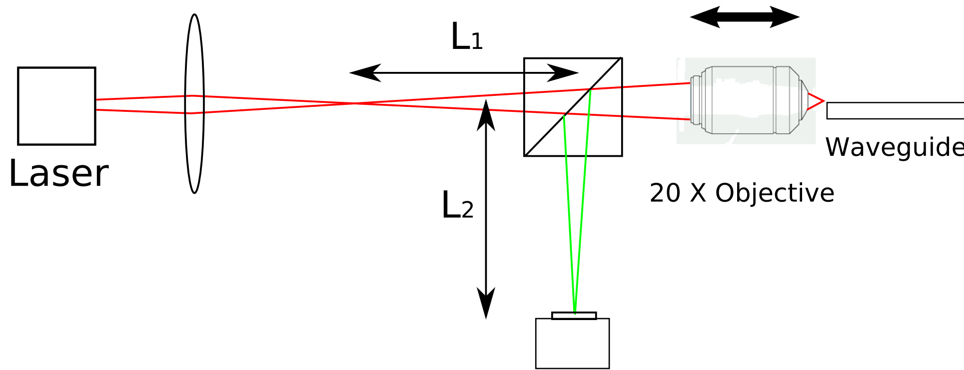

Figure 5.8: A variation of the basic in-coupling system.

5.5 Modified Illumination System

Since the working distance of the out coupling objective is quite small (order of 1 *mm*), the extra illumination that we use from the top of waveguide is not always suitable to light up the back facet of waveguide. This kind of illumination, which needs to be at a particular angle with respect to the back facet, sometimes causes diffraction effect (See Fig. 5.7(a) or Fig. 5.9). With this diffraction effect, it is hard to tell where the top surface of the waveguide exactly is. In order to get rid of this effect, and get a clear image of back facet of the waveguide, I use an extra He-Ne laser in combination with a lens with large focal length (200 *mm*) and a beam splitter to build a illumination system for the back facet. The collimated He-Ne laser beam (indicated in red in Fig. 5.10) is converged by the moveable 200 *mm* lens first. Then it is reflected by the beam splitter, which is fixed between the out-coupling objective and the Apogee imaging CCD. The beam splitter is well adjusted such that the reflected He-Ne beam goes perpendicularly through the objective lens and eventually hits the facet. By moving the 200 *mm* lens longitudinally with respect to the He-Ne beam, the location of the focus can be adjusted and the beam size at the facet of the waveguide can be enlarged. As a result, a large area of the back facet is lighted up by the He-Ne laser (Fig. 5.10).

The light from the waveguide facet (indicated in blue in Fig. 5.10), on the other hand, is still focused on the Apogee CCD because the beam splitter in between merely changes the optical length compared to the distance between the objective and Apogee camera. Therefore, since we got a clear image of the waveguide facet before, we also can get a sharp image with this home-made illumination system. Fig. 5.11 is an image of the test waveguide facet from Gregory obtained with this system. The diffraction pattern visible in Fig. 5.9 has disappeared and the top surface of this waveguide is clearly visible.

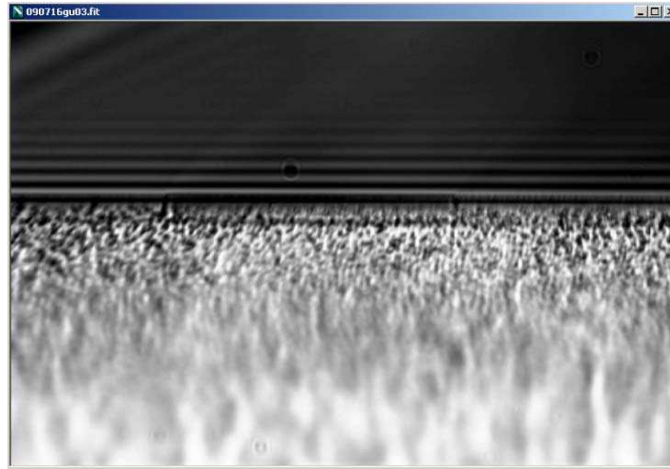

Figure 5.9: Magnified image of the back facet of a waveguide. The facet is lighted up by using an extra white source illumination. A surprising and unexpected diffraction pattern appears in this image.

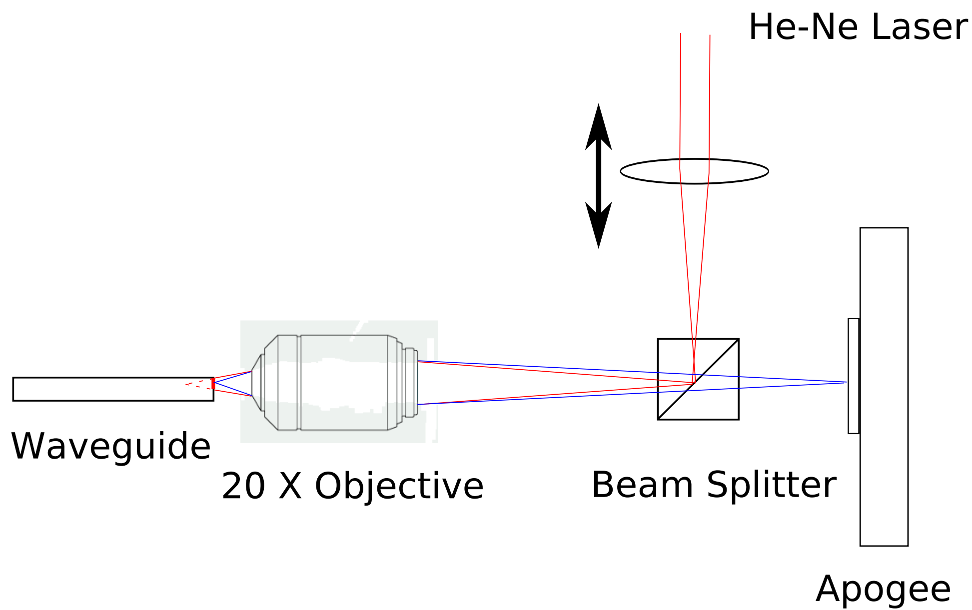

Figure 5.10: A home-made illumination system by using an extra He-Ne laser.

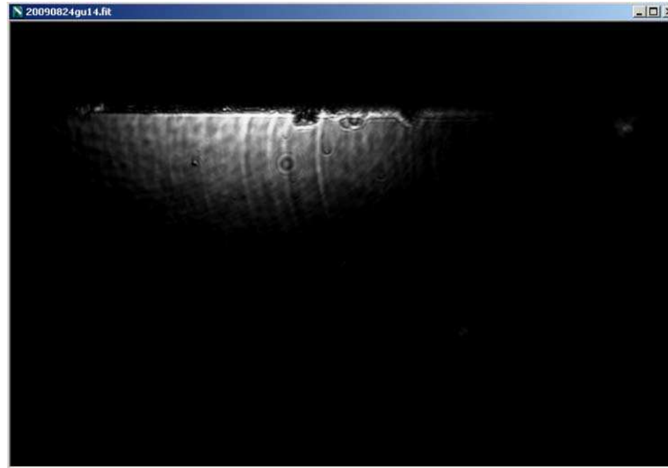

Figure 5.11: An image of the back facet of Gregory's wafer, using the illumination system designed in Fig. 5.10. The bright area is the facet of the waveguide which is lighted up by the He-Ne laser beam. In this figure, the interface between the waveguide and the air (the dark region on top of the bright area) is clearly distinguishable. Also, we can adjust the size of the bright area by moving the movable lens along its optical axis. Two defects at the facet are shown on the right side of the bright region, which means that the facet is not perfect.

5.6 Result obtained by the out-coupling system

When the in-coupling infrared laser is switched on, a 2-point pattern, which does not have any explanation yet, is captured by the Apogee camera that looks at a magnified image of the back facet of the waveguide (See Fig 5.12). The distance between these two points is 116.6 *um*, and this kind of pattern does not depend on the size of the rib, because it shows up when either single 100 *um* rib or a pair of 5 *um* ribs is investigated, and the distance between these two points are exactly the same for every kind of waveguide. Actually, the same pattern is still observed from the back facet even if the in-coupling beam is focused on the slab structure rather than the rib. So this 2-point pattern does not depend on the waveguide at all.

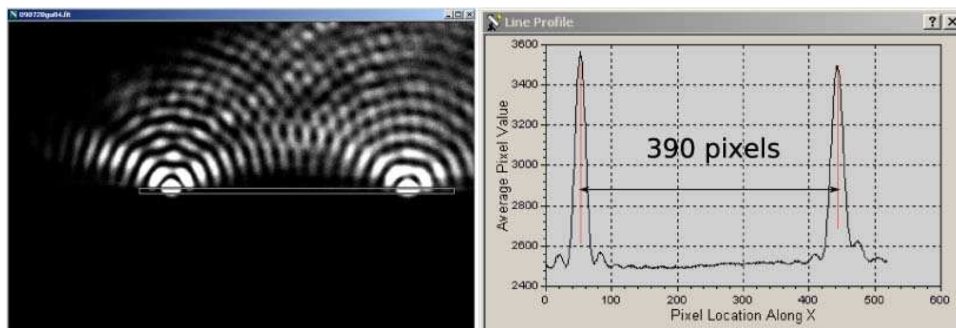

Figure 5.12: The 2-point pattern that can not be understood.

These 2-point pattern have a strange behavior if I move the in-coupling objective lens downwards. Fig. 5.13 includes a series of images which shows how the pattern changes when the objective is moved from top to down. Fig. 5.13 (a) is the starting point where the 2-point pattern just shows up. If the in-coupling objective is moved down, these two points move down to a lowest level (Fig. 5.13 (b)) that they can reach. Keeping moving the objective down, however, the points move up again (Fig. 5.13 (c)). If I still move the in-coupling beam down, the two points disappear and fringes in between them appear instead (Fig. 5.13 (d)). After that the fringes change from Fig. 5.13 (e) to Fig. 5.13 (g). Doing the integral over the whole image, the total intensity collected by the out-coupling system is shown in Fig. 5.14. From this figure we can see that the total intensity is much larger in Fig. 5.13

(e) and (f) than in other images. In Fig. 5.13 (h), the intensity of the light is much lower than that in previous images, and also it is irregular. This is because the full in-coupling beam is firing onto the Si substrate. Fig. 5.13 (i) is a reference image shot under extra illumination of the back facet. Comparing this image with others, one can find that all the light detected before is above the surface of the waveguide, but not on the surface and therefore not due to out coupling. It is very strange that from Fig. 5.13 (a) to (h), the objective is moved downwards from the surface plane of the waveguide by more than 15 um before the entire beam is on the substrate. But the thickness of the $SiN + SiO_2$ layer is only 2.2 um. How could the focus of the beam travel so much distance before it moves onto the silicon while we know that the beam is focused on the front facet? There is a small possibility that the incident beam was not properly focus on the front facet, but even that the obtained results are strange.

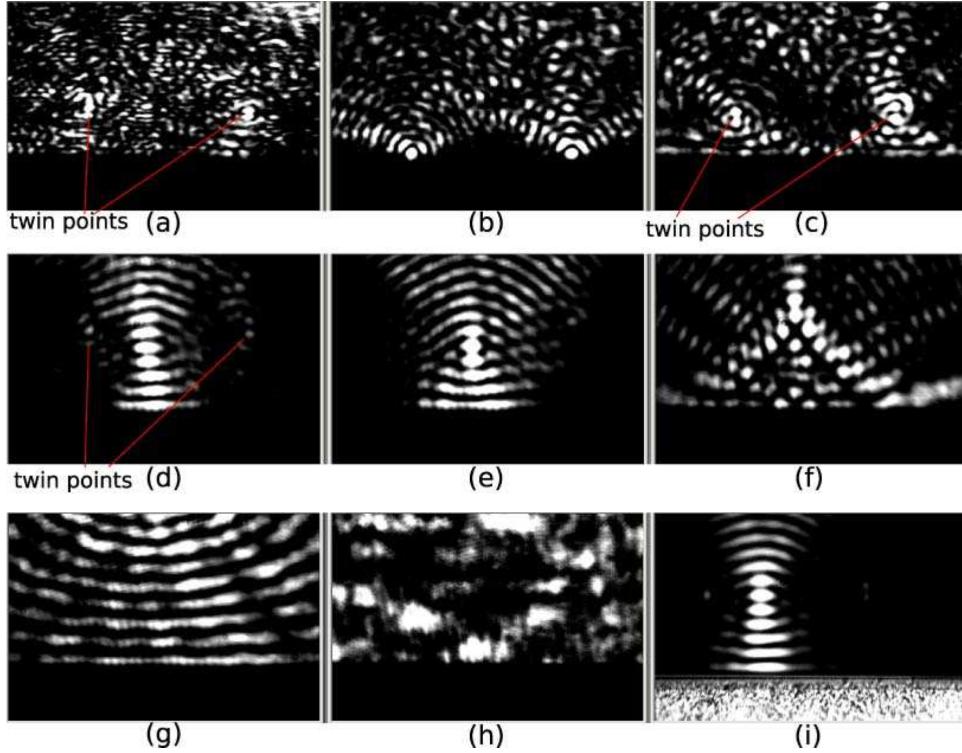

Figure 5.13: A series of images which show how the intensity pattern behind the waveguide changes when the laser beam is moved downwards.

5.7 Large Single-mode Rib Waveguide

5.7.1 Success in the large scale waveguide

The waveguide with the scale shown in Fig. 3.22, given by Gregory for testing our system, meets equation (5.2). Therefore, it is actually a single-mode waveguide. Because the waveguide is quite large, compared with the waveguide we used before, coupling is relatively easy. Actually we succeeded in coupling light into the waveguide at the first try. The proof of this is given in Fig. 5.16(a), which is captured by an analog video camera looking from the top.

Calibration of the video camera

The analog video camera we use to inspect the waveguide from the top is equipped with a highly magnifying lens mounted above the waveguide. The video camera is calibrated as below. Firstly, I adjust the translational stage, on which the video camera is mounted, and get a image shown in

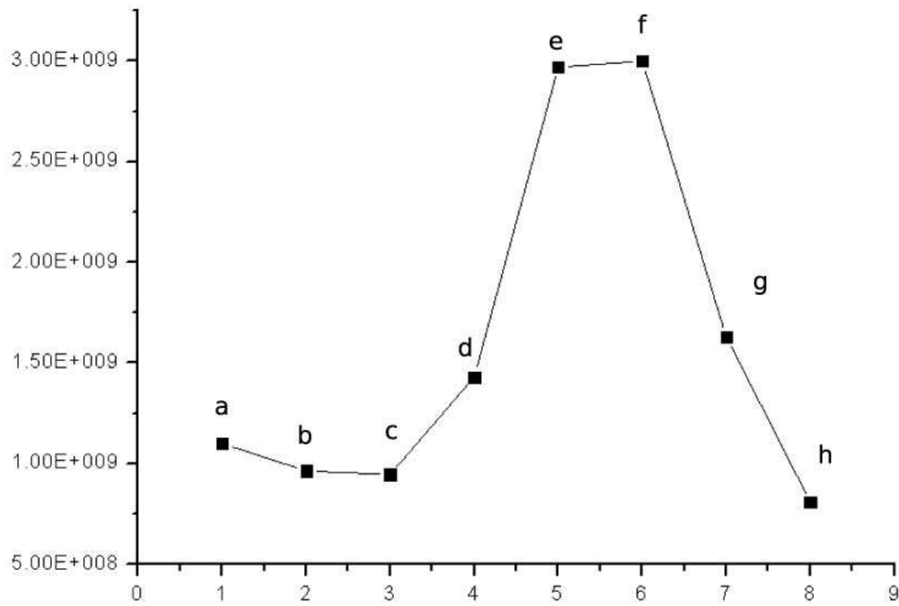

Figure 5.14: .

Fig. 5.15(a). I use the right edge of the top bright line (rib structure) as a mark, and record the horizontal pixel number of it in the following images. Moving the camera 0.5 *mm* to the right, the waveguide moves to the left of the image. And the pixel value of the marked point moves from 268 to 217. Redoing this step for another 4 times, and the pixel value of that point moves to x, 118, 67, 17 measured in Fig. 5.15 (c), (d), (e), (f) (x is unknown because 5.15 (c) is lost by mistake). In conclusion, a displacement of 0.5 *mm* leads to 50 pixels change in the image of the video camera. So the pixel size of this camera is 10 *um*

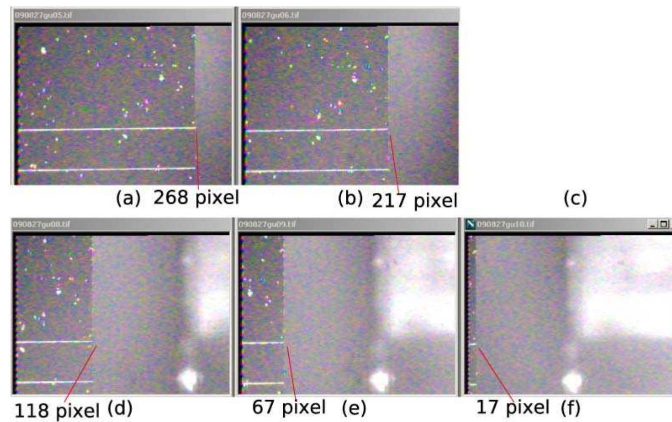

Figure 5.15: A series of images captured by a video camera. Between every two images the camera is moved by 0.5 mm. Image (c) is lost by mistake.

Result on this waveguide

Fig. 5.16 shows a group of images of Gregory's (test) waveguide captured by the video camera looking from the top. The image is colorful and quite noisy because the video camera is analog. When we convert the analog signal to digital with a frame grabber , noise comes out. In Fig. 5.16(a), we can see that the rib structure is lighted up by the laser. We believe this phenomena corresponds to the coupling, because if I move the beam about 3 *um* left, the rib is not lighted up. (Fig. 5.16 (b)). And the same is true for moving the beam 3 *um* right (Fig. 5.16 (c)). And if I move the beam really far from the rib structure, only a small part of the waveguide is lighted up by the laser (Fig. 5.16

(d)). Converting these images to monocolour to minimize the noise, the intensity profile of them are shown in Fig. 5.17. This allows us to roughly estimate that the length of the bright line in Fig. 5.16 (a) is 2.7 mm, while it is only approximately 1 mm in (d). So it seems that the energy is confined along the rib in (a). Using exponential decay fit ($exp(-x/L)$), the decay length L of the lighted up line in Fig. 5.16(a) is calculated to be 1.14 mm. The decay length obtained from the figures with displaced coupling (Figs 5.16(b)-(d) and 5.17(b)-(d))is noticeably shorter. Therefore, coupling is the only explanation for this long bright line. The reason why only 3 mm rib structure can be seen must be that the waveguide is quite lossy.

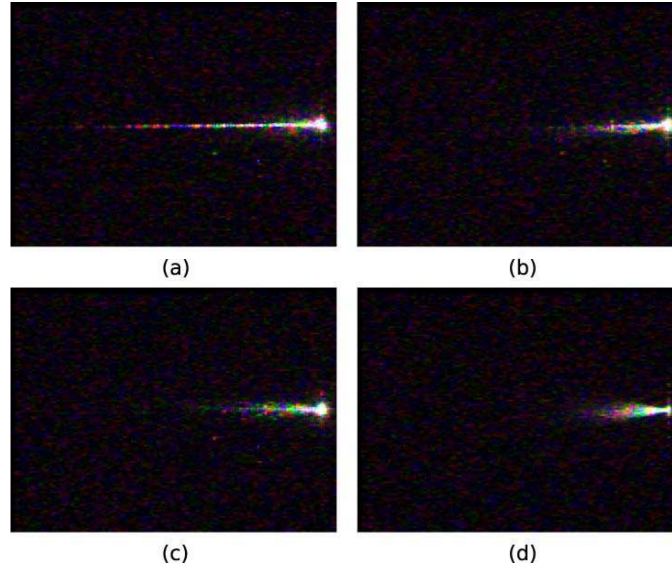

Figure 5.16: A series of images captured by the top video camera when I focus the beam (a) on the rib, (b) 3 um left, (c) 3 um right and (d) far away from the rib.

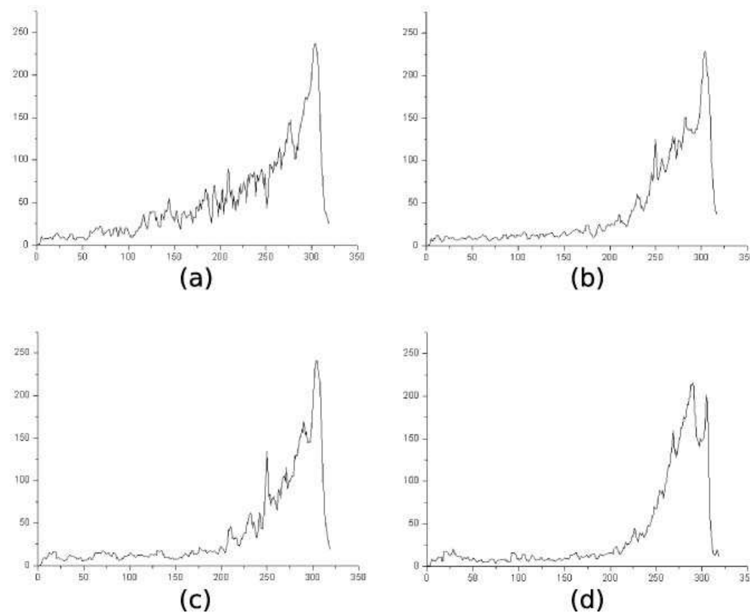

Figure 5.17: Intensity profile along the lighted up parts of Figure 5.17.

Another proof that we success in coupling comes from the back facet. In Fig. 5.18, there is a small bright spot inside the red circle. And the intensity profile along the green dashed line is shown on the right.

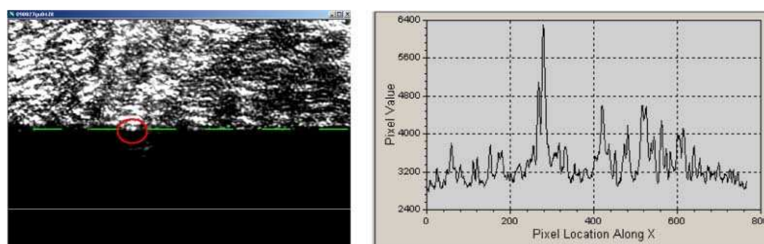

Figure 5.18: A image of back facet of the test waveguide corresponding to when we see the 3 mm long bright line in Fig. 5.16 (a) and 5.17(a) and 5.17(a).

Chapter 6

Summary

This thesis summarizes our characterization of three different waveguide structures and our efforts to couple light into and out of these waveguides. We have studied: (1) Planar waveguides of 0.2 micron thick SiN on SiO_2; (2) Rib waveguides which are made by etching SiN layer of the first kind of waveguide down by 50 nm; and (3) Large single-mode rib waveguides which are made from SiC on SiO_2.

Characterization of these waveguides with an optical microscope and a scanning electron microscope gave the following results: the free-standing SiN films of 2-D planar waveguides is a little different from what we expected, while those of the 1-D planar waveguides are quite good. By using the normal interference and low-coherent interference methods, both the continuous and stepwise height profiles can be measured. With the electron microscope, the quality of the facet can be inspected.

When we failed to couple light into simple planar waveguides, we switched to rib-type waveguides that are supposed to guide light in a thin line across the full wafer. Instead of the expected small bright spot at the back facet, a series of intriguing but unexplained interference patterns are detected.

We have developed several alignment procedures and tried to optimize the illumination and imaging system. We believed that we succeeded in coupling light into the large scale rib waveguide. However, the light propagates only several millimeters. Although this light could be easily observed from the top of the wafer it was hardly visible from the back facet, being overwhelmed by light originating from other scattering processes.

One of the reason for our failure to efficiently couple light into the waveguide might be the existence of an ≈ 10 um wide free-standing film of SiN on the etched edges of our samples (See Fig. 3.21). This unexpected structure is caused by the (wet) KOH etching that is applied to the wafer before sawing.

I would like to end with the following suggestions for future experiments: (1) For planar waveguides, prism coupling and grating coupling could be more effective than end-fire coupling; (2) Improve the etch and cut technique that is now used to slice up the wafer; (3) Single-mode rib waveguides can also be made several microns thick, thus allowing more efficient in-/out- coupling, with loosing their single mode character if one uses the proper ratio of rib width to rib height; (4). A disadvantage of the Elliot scientific alignment stage is the absence of an absolute scale. Such a scale is desirable for future experiments; (5) Keeping more books about waveguiding in the library and having free access to IEEE Journal would be very helpful for the research.

Bibliography

[1] A. Yariv, *Quantum Electronics, 3rd Edition* (John Wiley & Sons, 1975).

[2] H.J. Eom, *Electromagnetic Wave Theory for boundary-Value Problems* (Springer, 2004).

[3] B.E.A. Saleh, M.C. Teich, *Fundamentals of Photonics, 2nd Edition* (John Wiley & Sons, 2007).

[4] D. J. Griffiths, *Introduction to Electrodynamics* (Prentice Hall, 1996).

[5] Graham T. Reed, Andrew P. Knights, *Silicon photonics: an introduction* (Wiley, 2004).

[6] P. K. Tien, R. Ulrich, R. J. Martin, *Modes of Propagating light waves in thin deposited semiconductor films*, Applied Physics Letters, Vol. 14, No. 9, Pages 291-294, 1969.

[7] J. M. Hammer, D. J. Channin, M. T. Duffy, C.C Neil, *High-Speed Electrooptic Waveguide Grating Modulator Using Epitaxial ZnO*, IEEE Journal of Quantum Electronics, Vol. QE-11, No. 4, Pages 138-148, 1975.

[8] Chin-Lin Chen, *Foundations For Guided-Wave Optics* (John Wiley & Sons, 2006).

[9] W. C. L. Hopman, H. J. W. M. Hoekstra, R. Dekker, L. Zhuang, and R. M. De Ridder, *Far-field scattering microscopy applied to analysis of slow light, power enhancement, and delay times in uniform*, Optics Express, Vol. 15, No. 4, Pages 1851-1870, 2007.

[10] Zhechao Wang, Ning Zhu, Yongbo Tang, Lech Wosinski, Daoxin Dai, Sailing He, *Ultracompact low-loss coupler between strip and slot waveguides*, Optics Letters, Vol. 34, No. 10, Pages, 1498-1500, 2009.

[11] C. Pang, F. Gesuele, A. Bruyant, S. Blaize, G. Lerodel and P. Royer, *Enhanced light coupling in sub-wavelength single-mode silicon on insulator waveguides*, Optics Express, Vol. 17, No. 9, Pages, 6939-6945, 2009.

[12] Richard A. Soref, Joachim Schmidtchen, Klaus Petermann, *Large Single-Mode Rib Waveguide in GeSi-Si and Si-on-*SiO_2, IEEE journal of Quantum Electronics, Vol. 27, No. 8, Pages, 1971-1974, 1991